NANOROBOTS

Tracking and navigation of a microswarm under laser speckle contrast imaging for targeted delivery

Qinglong Wang[1]†, Qianqian Wang[2]*†, Zhipeng Ning[1], Kai Fung Chan[3,4], Jialin Jiang[1], Yuqiong Wang[1], Lin Su[1], Shuai Jiang[1], Ben Wang[5], Bonaventure Yiu Ming Ip[6]*, Ho Ko[6], Thomas Wai Hong Leung[6], Philip Wai Yan Chiu[3,4,7], Simon Chun Ho Yu[8], Li Zhang[1,3,4,7,9]*

Micro/nanorobotic swarms consisting of numerous tiny building blocks show great potential in biomedical applications because of their collective active delivery ability, enhanced imaging contrast, and environment-adaptive capability. However, in vivo real-time imaging and tracking of micro/nanorobotic swarms remain a challenge, considering the limited imaging size and spatial-temporal resolution of current imaging modalities. Here, we propose a strategy that enables real-time tracking and navigation of a microswarm in stagnant and flowing blood environments by using laser speckle contrast imaging (LSCI), featuring full-field imaging, high temporal-spatial resolution, and noninvasiveness. The change in dynamic convection induced by the microswarm can be quantitatively investigated by analyzing the perfusion unit (PU) distribution, offering an alternative approach to investigate the swarm behavior and its interaction with various blood environments. Both the microswarm and surrounding environment were monitored and imaged by LSCI in real time, and the images were further analyzed for simultaneous swarm tracking and navigation in the complex vascular system. Moreover, our strategy realized real-time tracking and delivery of a microswarm in vivo, showing promising potential for LSCI-guided active delivery of microswarm in the vascular system.

INTRODUCTION

Micro/nanorobots harvest energy from internal or external environments to achieve active motion. This characteristic behavior of micro/nanorobots permits biomedical applications, especially in endovascular systems, such as thrombus removal, wound healing, and drug delivery, because of their tiny size and controllable locomotion (*1*–*8*). To ensure delivery efficiency and biomedical safety in complex vascular environments, real-time imaging of micro/nanorobots is essential (*9*–*12*). In recent years, various imaging modalities have been applied for the imaging of micro/nanorobots, including magnetic resonance imaging (MRI) (*13*, *14*), ultrasound (US) imaging (*15*, *16*), fluorescence imaging (*17*, *18*), computed tomography (CT) (*19*, *20*), positron emission tomography (PET) (*21*), fluoroscopy (*22*, *23*), single-photon emission computed tomography (*24*), and photoacoustic imaging (PAI) (*25*, *26*). In table S1, we summarized the pros and cons of common imaging modalities for the imaging of micro/nanorobots in terms of penetration depth, spatial resolution, and temporal resolution. In short, ionizing radiation–based techniques, such as CT, PET, and fluoroscopy, have excellent tissue penetration. However, radiation risk is the main concern when conducting therapeutic intervention over a long duration. MRI has the advantage of high penetration depth in tissues; however, the low temporal resolution (minutes-hours) renders difficulties in tracking the micro/nanorobots in real time. PAI is an emerging imaging tool that enables real-time imaging and tracking in deep tissues. However, imaging and tracking of micro/nanorobots in vascular systems with complex branching and hemodynamics by PAI require further validation. More recently, optoacoustic tomography has been reported for tracking individual microrobots in the vascular system with magnetic manipulation (*27*). Nonetheless, imaging of micro/nanorobots is restricted within the endovascular system because of the tiny size of micro/nanorobots and distributed imaging signals. To tackle this issue, inducing swarm behaviors of micro/nanorobots is an effective solution, which can improve the pattern area density and imaging contrast because of the active gathering effect and swarm-environment interactions. For instance, Wang *et al.* (*28*) applied US imaging to track a magnetic microswarm in the endovascular environment. Duplex US with B-mode and Doppler mode is able to visualize microswarms in the bloodstream. Although US imaging has relatively strong penetration in soft tissue and is noninvasive, the restricted acoustic window in the endovascular lumen and relatively low signal-to-noise ratio of US may result in signal loss, causing difficulty in distinguishing the micro/nanorobotic swarm from the dynamic environments. Therefore, a noninvasive, real-time, full-field imaging method with a high temporal-spatial resolution that can track swarming micro/nanorobots and swarm-environment interactions is needed to promote targeting ability and delivery efficiency.

A micro/nanorobotic swarm increases delivery efficiency with enhanced imaging contrast, pattern transformation rate, and environmental-adaptive capability, thus improving the efficiency of endovascular interventions (*10*, *29*–*35*). For instance, swarming micro/nanorobots with enhanced drug delivery accelerate thrombolysis endowed by swarm-induced hydrodynamic convection (*36*, *37*). Quantitative investigation of swarm-environment interactions in the blood may further enhance the current understanding of micro/

[1]Department of Mechanical and Automation Engineering, Chinese University of Hong Kong (CUHK), Shatin, N.T., Hong Kong, China. [2]Jiangsu Key Laboratory for Design and Manufacture of Micro-Nano Biomedical Instruments, School of Mechanical Engineering, Southeast University, Nanjing, China. [3]Chow Yuk Ho Technology Centre for Innovative Medicine, CUHK, Shatin, N.T., Hong Kong, China. [4]Multi-Scale Medical Robotics Center, Hong Kong Science Park, Shatin, N.T., Hong Kong SAR, China. [5]College of Chemistry and Environmental Engineering, Shenzhen University, Shenzhen, China. [6]Division of Neurology, Department of Medicine and Therapeutics, CUHK, Shatin, N.T., Hong Kong, China. [7]Department of Surgery, CUHK, Shatin, N.T., Hong Kong, China. [8]Department of Imaging and Interventional Radiology, CUHK, Shatin, N.T., Hong Kong, China. [9]CUHK T Stone Robotics Institute, CUHK, Shatin, N.T., Hong Kong, China.
*Corresponding author. Email: qqwang@seu.edu.cn (Qianqian Wang); bonaventureip@cuhk.edu.hk (B.Y.M.I.); lizhang@cuhk.edu.hk (L.Z.)
†These authors contributed equally to this work.

nanorobotic swarm behavior and strengthen their capabilities in different biomedical applications. Restricted by current methodologies, studies that quantitatively analyzed hydrodynamic convection and its associative factors are scarce. Developing alternative methods that are able to address these issues may improve swarm controllability and delivery efficiency, which are vital for safe and efficacious endovascular procedures.

Laser speckle contrast imaging (LSCI) can monitor the changes in the bloodstream within the area of interest without the requirement of scanning in a real-time manner, which has been applied to assess reperfusion status after ischemic stroke (*38*–*40*). Laser speckle is a physical phenomenon induced by light interference on particles or coarse surfaces (*41*, *42*). When laser light irradiates red blood cells (RBCs), it scatters and generates coherent scattering light. An alternating pattern of light and dark will then be formed from random interference of the scattered light. Such a pattern is named "speckle," which can be influenced by the movement of RBCs. The movement of RBCs blurs the speckle pattern, resulting in a change of speckle contrast. Velocity distributions of the diffuse objects can, therefore, be coded as speckle contrast variations. The speckle contrast variations are then analyzed and displayed as speed-related images. On the basis of the imaging mechanism of LSCI, we hypothesized that a microswarm constructed by numerous nanoparticles would generate imaging signals by interaction with RBCs. Furthermore, simultaneous visualization of RBCs movement allows quantification of the interaction between a micro/nanorobotic swarm and the surrounding blood environment, which may facilitate the targeted delivery process.

Here, we report a LSCI-based swarm tracking method to navigate a microswarm in endovascular environments with real-time monitoring (Fig. 1A). Fe_3O_4@SiO_2 nanoparticles with a diameter of 300 to 400 nm (fig. S1) were used as the tiny building blocks. A sphere magnet was applied to generate a rotating magnetic field, which can control the microswarm formation and navigation process. In stagnant blood environments, the microswarm showed a relatively strong imaging contrast in both the pseudo-color pattern and the gray pattern (Fig. 1B). The hydrodynamic convection generated by the rotating motion of the microswarm effectively agitated surrounding RBCs. The movement of RBCs was detected by LSCI and transformed into imaging signals. Two types of imaging modes, pseudo-color pattern and gray pattern, were captured. Compared with the gray pattern in stagnant blood, the pseudo-color pattern exhibited a better imaging profile and provided more details in the contrast change. In flowing blood, the microswarm showed a smaller imaging profile (Fig. 1B). The microswarm mainly exhibited an imaging profile of itself in the dynamic environment, which was distinguished by the difference in imaging contrast between the microswarm and the bloodstream. The gray pattern was more suitable for the flowing conditions because of the differentiation between the microswarm and surrounding RBC signals. Moreover, the hydrodynamic convection could be evaluated by the motion of RBCs, and quantitative analysis was achieved by monitoring the perfusion unit (PU) change. Such an exclusive feature allowed us to optimize the parameters to improve hydrodynamic convention and benefit the delivery process. Our work presents a noninvasive and high-resolution approach for the tracking and navigation of a microswarm in an endovascular system with a large imaging field that allows real-time feedback.

RESULTS

Imaging of a microswarm on a flat surface

The study of interactions between the micro/nanorobotic swarm and the surrounding environment may enhance the fundamental understanding of in vitro and in vivo behaviors of the micro/nanorobotic swarm and thereby promote its applications. However, common preexisting imaging tools may not achieve this goal because of the restrictions discussed above. Here, we investigated the imaging of the microswarm on a flat surface with whole blood to explore the interaction between the microswarm and the surrounding environment. Figure 2A shows a schematic illustration of the imaging mechanism of a magnetic microswarm on a flat surface, which enables imaging signals by induced moving RBCs. A sphere magnet was used to generate a rotating magnetic field, where magnetic nanoparticles formed the circular microswarm by dipole-dipole interaction and magnetic field gradient. The relationship between the distance (the distance between the magnet tip and the swarm plane) and the magnetic field strength is offered (fig. S2). Figure S3 describes a representative microswarm with a diameter of around 2.5 mm, and the microswarm also shows an imaging profile without blood. The rotation motion of magnetic chains of the microswarm induced hydrodynamic convection, resulting in the movement of surrounding RBCs. The displacement of RBCs was then captured and transformed into imaging signals by LSCI. Therefore, the imaging of the microswarm was inferred by detecting the movement of RBCs. The imaging mechanism was further verified by simulation (Fig. 2B). We released 3000 microparticles as the simulated RBCs that had the same diameter and density as

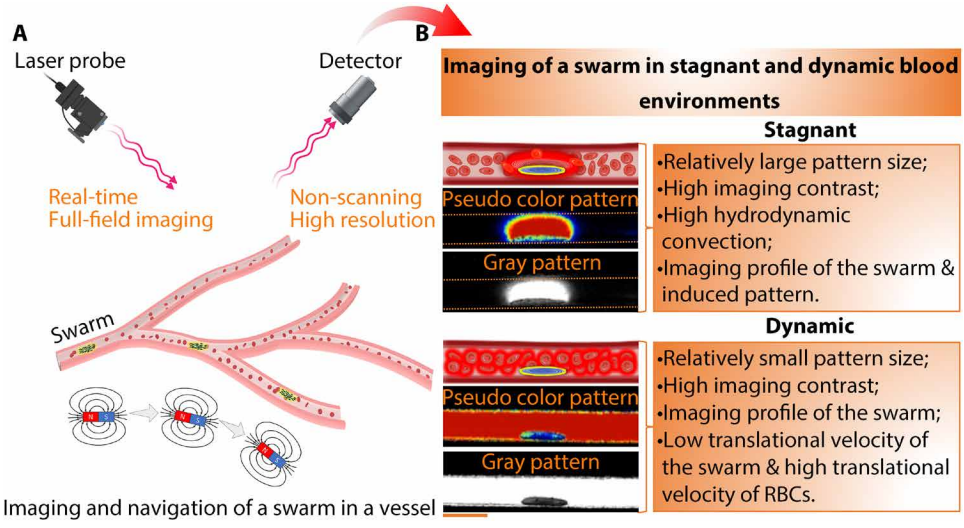

Fig. 1. Schematic illustration of LSCI-based real-time tracking of a microswarm. (**A**) Schematic illustration of the imaging and navigation of a magnetic microswarm in a blood vessel. (**B**) Photographs depict the real imaging of a magnetic swarm in the vessel with both stagnant and flowing blood. Scale bar, 5 mm.

human RBCs. The blue lines illustrate motion trajectories of the simulated RBCs around the microswarm, suggesting that RBCs are disturbed around the microswarm by the pattern-induced convection. Moreover, the hydrodynamic convection was higher around the center of the microswarm, which led to faster movement of RBCs and stronger imaging signal intensity. The simulation of the state of the microswarm and simulated RBCs at time $t = 10$ s is illustrated in fig. S4, showing the movement of RBCs toward the microswarm center. Figure 2C shows the formation process of a magnetic microswarm monitored by LSCI. The imaging pattern of the microswarm gradually transformed from an irregular shape into a circular shape, indicating successful generation of the microswarm. In comparison, no imaging signals were observed for the stationary microswarm without hydrodynamic interaction with RBCs (fig. S5). The last photograph in Fig. 2C shows the reducing image signal intensity away from the swarm center, which was in concordance with the simulation results. Moreover, the imaging signal of spread nanoparticles was weaker than that of the microswarm, indicating that enhanced imaging signal intensity is obtained by the collective behavior of the microswarm.

To quantitatively study the imaging signal intensity and hydrodynamic convection induced by the microswarm, the PU that represents the change in blood flow is introduced. Here, the PU value is calculated as

$$\mathrm{PU} = \frac{1}{K^2} \tag{1}$$

where the K refers to speckle contrast value, which is defined as the ratio between the SD of speckle intensity and mean of speckle intensity, described as (*42*)

$$K = \frac{\sigma}{\langle I \rangle} \tag{2}$$

where the σ refers to the SD of speckle intensity and I indicates the mean of speckle intensity. On the basis of the dynamic light scattering approximate model, the speckle contrast value K can be expressed as a function of the coherent light decorrelation time τ_c (*43*)

$$K = \sqrt{\frac{\tau_c}{2T}\left[1 - \exp\left(-\frac{2T}{\tau_c}\right)\right]} \tag{3}$$

where T is the speckle imaging exposure time. When $T \gg \tau_c$, the speckle contrast value K shows a square root dependence relationship with τ_c. The relationship between τ_c and the velocity v_c of the scattering particles can be expressed as (*42*)

$$v_c = \frac{\lambda}{2\pi\tau_c} \tag{4}$$

where λ is the wavelength of coherent light. When $T \gg \tau_c$, the laser speckle contrast value K is inversely proportional to the square root of the velocity v_c of the scattering particles. Therefore, PU is proportional to the velocity v_c of the scattering particles (RBCs in our study). Moreover, the PU and mean flow velocity are positively related (fig. S6). The changes in PU and imaging area were investigated with different factors, including input frequency, nanoparticle dose, blood depth, and distance between the magnet tip and the swarm plane.

In Fig. 2D, the PU increased notably with the increase in applied field frequency, reaching the highest value of around 115 with the input frequency of 7 Hz. The imaging area was also gradually enlarged with input frequency, and two factors were attributed to the change of imaging area: The range of influenced RBCs became larger with stronger hydrodynamic convection, and the microswarm was in a more dispersive state with relatively high frequency because of enhanced repulsion between magnetic chains, resulting in a larger swarm size. The imaging pattern of the microswarm with various frequencies is shown in Fig. 2J, where both imaging intensity and imaging area were enhanced with increasing input frequency. On the basis of the observed changes in PU value change, the hydrodynamic convention can be controlled by adjusting magnetic field frequency, potentially facilitating the drug delivery process. Similar to the influence of input frequency, both the PU value and the imaging area of the microswarm were continually enhanced by increasing the nanoparticle dose, whereas the improvement of PU was limited as the dose exceeded 100 μg (Fig. 2E). The patterns of the microswarm with various doses of nanoparticle (10, 20, 40, 60, 80, 100, and 200 μg) were investigated (fig. S7). Another factor that affected the PU and imaging area was blood depth, revealing the ability of the microswarm to trigger vertical hydrodynamic convection. As shown in Fig. 2F, PU value and imaging area declined with the increase in blood depth. The values of PU and the imaging area decreased from 118 to 42 and 55 to 10 mm^2, respectively, as blood depth increased from 1.0 to 3.5 mm. The imaging of the microswarm at different blood depths displayed in Fig. 2I further substantiated the decreased signal intensity and imaging area as depth increased. The maximal blood depth that the microswarm could influence was 3.5 mm, and the signal became vague when the blood depth was beyond 3.5 mm. LSCI shows advantages compared with optical-based imaging modalities, which offers an opportunity to explore the swarm-environment interaction in the deeper blood environment. With increasing distance from the magnet tip and the swarm plane, we found that the values of PU and the imaging areas were first enlarged and then gradually reduced (Fig. 2G). The microswarm generated the strongest LSCI signals with a distance of 10 mm, as shown in Fig. 2G. The influence of the distance on the imaging pattern is further depicted in fig. S8.

To comprehensively study the change of hydrodynamic convection, the PU distributions over the microswarm were recorded and analyzed. Figure 2K demonstrates the PU distribution over the microswarm with different frequencies, and the range that the microswarm can affect was observed. The PU change resembled a normal distribution, where the PU continuously declined from the center of the microswarm, demonstrating that higher hydrodynamic convection was induced close to the swarm center. Besides, the PU distribution of the microswarm with various nanoparticle doses was explored (Fig. 2L). Enhanced imaging range and PU value were shown in the distribution lines as nanoparticle dosage increased, with the highest PU value appearing around the microswarm center. The hydrodynamic convection triggered by the microswarm can be quantitatively assessed by PU change, and optimized parameters were obtained to improve the pattern-environment interaction. Moreover, direct imaging of the microswarm could be achieved by LSCI in a water-glycerin solution with a viscosity of 4.5 centipoise (cp) that mimics the viscosity of the whole blood (*15*), which could directly reflect real microswarm behavior. The influences of different factors, including input frequency, nanoparticle dose, distance, and angle, were analyzed (figs. S9 to S12). Our results suggested that the microswarm behavior was consistent in environments with or

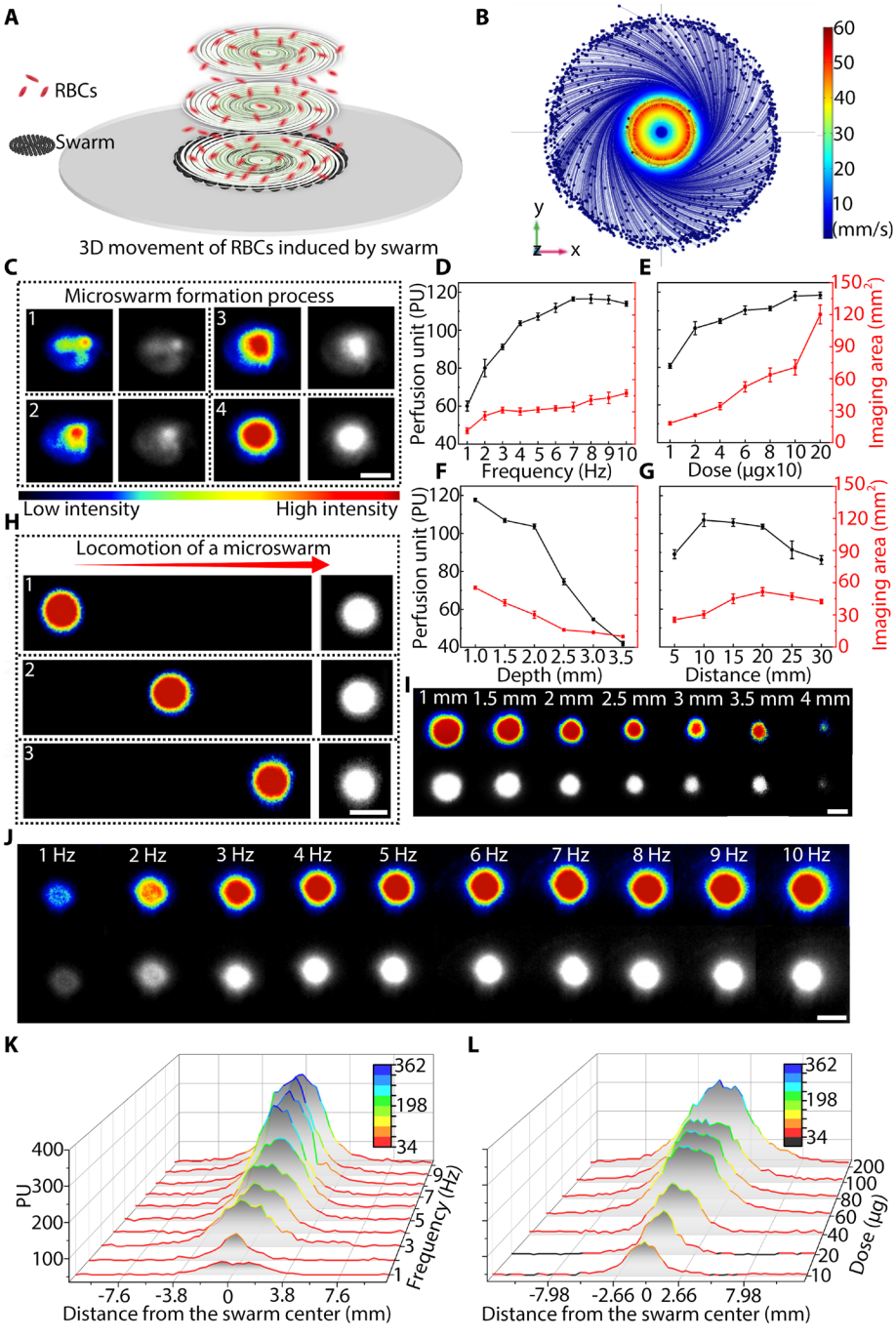

Fig. 2. Real-time imaging of a microswarm on a flat surface with whole blood. (**A**) Schematic illustration of a microswarm formed on a flat surface with whole blood. (**B**) Simulation result of the trajectories of simulated RBCs around the microswarm. Three thousand simulated RBCs were analyzed. The blue dots refer to the simulated RBCs (6-μm-diameter microparticles), and the blue lines donate the trajectories of the simulated RBCs. The color bar indicates the particle velocity. (**C**) The video clips (movie S1) show the microswarm formation process with pseudo-color patterns and gray patterns. (**D** to **G**) PU and imaging area of the microswarm vary with input frequency, nanoparticle dose, blood depth, and distance between the magnet tip and the swarm plane. All statistical results are based on three experimental tests, and the error bars represent the standard deviation (SD) of three experiments. (**H**) Translational locomotion of the microswarm on the flat surface with a velocity of 20 μm/s. The red arrow denotes the locomotion direction of the microswarm (movie S2). (**I** and **J**) Pseudo-color patterns and gray patterns of the microswarm with different blood depths and input frequencies. (**K** and **L**) Distribution of PU along the central line of the microswarm with different input frequencies and nanoparticle doses. The color bar donates the imaging signal intensity. Scale bars, 5 mm.

without RBCs. Furthermore, the reflectivity of the RBCs and magnetic nanoparticles (Fe_3O_4 and Fe_3O_4@SiO_2) was measured (fig. S13), which could reflect the light-scattering ability of the particles. The reflectivity of the RBCs substantially increased with wavelengths larger than 580 nm, whereas the reflectivity of Fe_3O_4 and Fe_3O_4@SiO_2 nanoparticles changed slightly over a wide range of wavelengths (250 to 900 nm). Figure S13B shows the reflectivity of three samples at the wavelength of 785 nm (the wavelength of the laser used in our work). Fe_3O_4 nanoparticles had the highest reflectivity of 72.4% and decreased to 65.4% after being coated with a SiO_2 shell. Moreover, the reflectivity of RBCs was 49.7% at a wavelength of 785 nm, which was lower than that of the two magnetic nanoparticles. It should be noted that the reflection spectra of particles in suspension are inversely correlated with absorption, suggesting that high reflection improves the LSCI imaging of particles. Therefore, LSCI is able to provide direct imaging of the magnetic nanoparticles because of their high reflectivity. Our results confirmed that the imaging of different nanoparticles with a wide range of reflectivity (49.7 to 72.4% in our study) can be achieved by LSCI.

Imaging-guided navigation of a microswarm in vessels

We further explored the imaging and navigation of the microswarm in the vessel with stagnant and flowing blood conditions. Figure S14 presents the schematic of the imaging of a microswarm in the vessel with a stagnant blood environment, and an imaging pattern with an ellipse shape was formed by applying a rotating magnetic field. The typical images with both the pseudo-color pattern and the gray pattern are exhibited in Fig. 3A, and the microswarm itself also shows an imaging profile due to the lower signal intensity compared with surrounding RBCs. In Fig. 3B, 3000 simulated RBCs were analyzed around the microswarm inside of the vessel. The motion trajectory of the simulated RBCs showed that more RBCs were captured near the microswarm because of the induced hydrodynamic convection, resulting in large imaging area and stronger imaging signals. The top view of the simulation for the trajectories of the simulated RBCs in the vessel with stagnant blood was conducted (fig. S15). The position of the microswarm inside of the vessel wall was controlled by adjusting the angle between the rotating

magnet and the *Z* axis of the tube. The influence of angle on the images was investigated (Fig. 3C). At 90°, the microswarm offered the best imaging, with a PU value of 215 and an imaging area of 18.94 mm^2, respectively. As the angle increased further, both the PU and imaging area were reduced accordingly. Moreover, the imaging profile of the microswarm itself became smaller with the increment of the angle (Fig. 3G, g1). The influence of the input frequency on the imaging of the microswarm was similar to that on the flat surface, and the PU notably increased with input frequency and reached the peak with an input frequency of 9 Hz (Fig. 3D). The imaging area change in the vessel became negligible when the input frequency was larger than 3 Hz, indicating that the microswarm was maintained at a stable state in the confined space. On the contrary, the PU was not sensitive to the dosage change (Fig. 3E) and was consistent at around 170 over a wide dose range (20 to 200 μg). On the other hand, a continuous increase in imaging area was observed, and the pattern size increased approximately twofold from 7.55 to 14.84 mm^2, as the dosage increased from 20 to 200 μg (Fig. 3, E and G, g3). The magnetic field strength was reduced with longer distances between the microswarm plane and the magnet tip. With increasing the distance, the PU value slightly raised and then dropped to around 160 because of the weakened hydrodynamic convection, whereas the imaging area gradually increased from 13.08 to 20.00 mm^2 (Fig. 3F). The microswarm was elongated in the vessel with increasing distance, which led to the enhanced area of the imaging pattern (Fig. 3G, g4). The imaging patterns of the microswarm with different angles, frequencies, and nanoparticle dosages are presented (figs. S16 to S18).

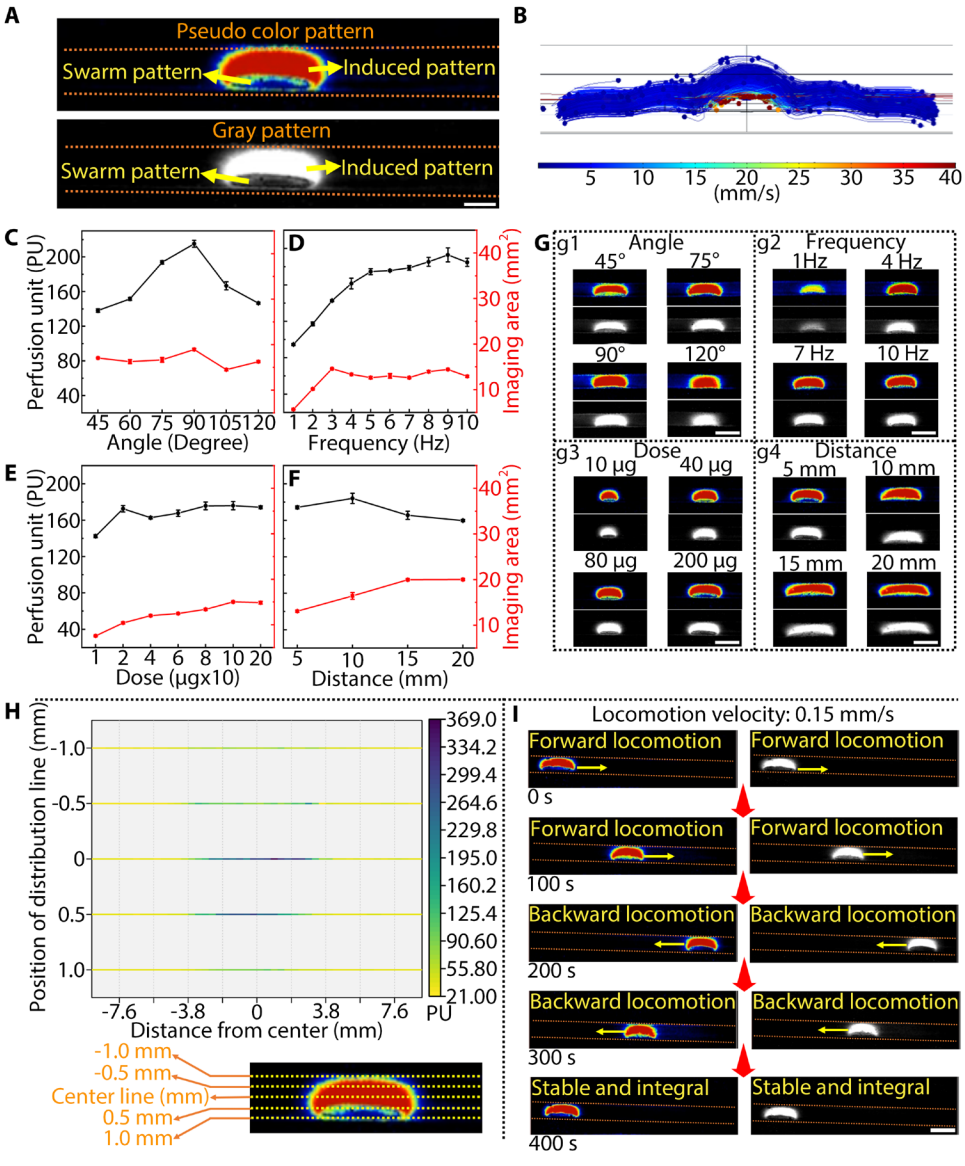

Fig. 3. Imaging and tracking of a microswarm in the vessel with stagnant blood. (**A**) Representative pseudo-color pattern and gray pattern of a microswarm in a silicone tube (inner diameter, 2 mm) with stagnant blood. The orange dashed lines refer to the profile of the tube edge. (**B**) Simulation of the RBCs' trajectories around the microswarm in the vessel with stagnant blood. The blue dots refer to the simulated RBCs, the blue lines donate the trajectories of the simulated RBCs, and the color bar indicates the particle velocity. (**C** to **F**) PU and imaging area of the microswarm vary with different input frequencies, nanoparticle doses, distances between the magnet tip and the swarm plane, and angles between the central axis of the magnet and the *Z* axis of the tube. All statistical results are based on three experimental tests, and the error bars represent the SD of three experiments. (**G**) Representative pseudo-color patterns and gray patterns of the microswarm with different input frequencies, nanoparticle doses, distances between the magnet tip and the swarm plane, and angles between the central axis of the magnet and the *Z* axis of the tube. (**H**) PU distribution of various distribution lines over the microswarm with an interval of 0.5 mm. (**I**) Navigation of the microswarm in the vessel with stagnant blood guided by LSCI (movie S3). The yellow arrows show the locomotion direction of the microswarm. Scale bars, 5 mm.

To investigate the PU distribution that can reveal the hydrodynamic convection change in detail, distribution lines with 0.5-mm intervals were chosen for analysis (Fig. 3H). A larger PU distribution was found close to the center of the microswarm, and the center line showed a higher PU value compared with the other four lines. Therefore, reinforced hydrodynamic convection was distributed around the center line. Moreover, the 1-mm line presented the imaging signal of the microswarm itself, and the PU value was located in the range of 50 to 107. The PU distribution showed that the microswarm itself was able to generate sufficient imaging signals except for interaction with RBCs. Subsequently, we verified the locomotion and navigation process of the microswarm in the vessel with stagnant blood. The forward and backward locomotion were guided by LSCI (Fig. 3I). During the locomotion process, both the microswarm and the imaging pattern remained stable and integral, suggesting that our control strategy was effective. The imaging and

tracking of the microswarm with different locomotion velocities were explored in movie S3; the microswarm with locomotion velocity lower than 0.5 mm/s remained intact without obvious nanoparticles lagging.

To investigate the imaging of the microswarm in dynamic environments, a peristaltic pump was deployed to control the blood flow in the silicone tube with an inner diameter of 2 mm. To reduce the influence of blood flow, the microswarm was magnetically navigated near the vessel wall, and the microswarm was able to resist against mean flow velocities of up to 110 mm/s. The schematic in Fig. 4A demonstrates the imaging signal of the microswarm in the flowing blood. As showcased in the typical imaging patterns (Fig. 4A), the microswarm exhibited blue and yellow color in the pseudo-color pattern and black color in the gray pattern because the signal intensity of the microswarm was lower than that of flowing RBCs. Compared with RBCs, the microswarm mainly performed in situ rotation motion, and the translational motion was too low to generate high imaging signal intensity. Different from the imaging of the microswarm in stagnant blood, the microswarm mainly showed the imaging profile itself; thus, the imaging size was relatively small. Therefore, adopting an optimized strategy to better visualize the microswarm in the flowing blood was necessary. We could optimize the imaging of the microswarm by controlling the angle between the magnet and the *Z* axis of the tube. The quantitative result (Fig. 4B) verified that the imaging area reduced from 2.89 to 1.55 mm^2 as the angle increased from 45° to 105°; thus, reducing the angle could improve the imaging area of the microswarm, as observed in Fig. 4F, f1. However, the angle cannot decrease indefinitely to avoid interference between the magnet and laser light, and the reasonable angle should be controlled in the range of 45° to 75°. Moreover, the PU value was maintained at around 95 over an angle range of 45° to 95° (Fig. 4B). In flowing blood, the input frequency influenced the PU value (Fig. 4C). The PU continuously increased from 82.8 to 108.3 as the input frequency increased from 1 to 10 Hz. Increasing the dose of nanoparticles was another method to improve the imaging area. An approximately 3.6 times increase in pattern size was observed as the dosage increased from 10 to 200 μg (Fig. 4D). Moreover, the value of PU and imaging area fluctuated with mean flow velocity from 5 to 110 mm/s (fig. S19). As a result, we confirmed the imaging of the microswarm in the vessel with flowing blood and further explored the optimal parameters for better visualization of the microswarm. The influence of different factors (angle, input frequency, dose, and mean flow velocity) on the imaging patterns of the microswarm was investigated (figs. S20 to S23).

Moreover, we also conducted the experiments using different magnetic nanoparticles, including Fe_3O_4, Fe_3O_4@SiO_2, Fe_3O_4@PDA, and Fe_3O_4@PDA@Au nanoparticles, to investigate the influence of the different components on the imaging of the microswarm. The transmission electron microscopy (TEM) images and magnetic hysteresis loop of those different nanoparticles were measured and compared (figs. S24 and S25). The results proved that the proposed strategy could visualize the microswarm with different components in various conditions using LSCI, enabling the elucidation of interaction between different magnetic microswarms and blood environments (fig. S26). Besides, comparisons between the real microswarm and the microswarm imaging were conducted to explore the behavior change of the microswarm with various factors to facilitate effective drug delivery. The change of the real microswarm size was summarized in table S2, and the influences of different parameters (input frequency, angle, nanoparticle dose, distance, and mean flow velocity) on microswarm size (real microswarm size and microswarm imaging size) and the ratio (microswarm imaging size/real microswarm size) were analyzed (figs. S27 to S30). Because the tissue environment is complex and penetration could be limited by tissue thickness, it is pertinent to study the maximal penetration depth by LSCI for microswarm imaging. The fetal membrane of a human placenta was used for imaging of the microswarm, where the tissue thickness can be determined by the number of tissue layers (fig. S31). The imaging signal intensity of the microswarm gradually reduced with increasing tissue layers. The results suggested that the behavior of the microswarm enables LSCI studies with a biological tissue thickness of 2.08 mm or below (fig. S32).

The locomotion ability of the microswarm in dynamic environments is critical for the delivery process. We demonstrated the downstream and upstream locomotion of the microswarm in the vessel with a mean flow velocity of 20 mm/s. The snapshots described the navigation process guided by LSCI, and the microswarm exhibited an imaging profile in both pseudo-color and gray pattern (Fig. 4G). The microswarm was capable of locomoting against relatively high blood flow, at the same time offering strong imaging signals for effective navigation that could facilitate the targeted delivery process. One feature of the microswarm is that the imaging contrast can be improved by localized imaging signals, which allows us to track the microswarm with a relatively low dose. In Fig. 4H, the microswarm with a dose of 20 μg showed good imaging contrast for tracking, and the LSCI-guided navigation process was accomplished with both downstream and upstream locomotion. Although the imaging profile may become blurred in the pseudo-color pattern (Fig. 4H), the gray pattern still showed strong imaging signals. Therefore, the gray pattern would be more suitable for imaging the microswarm in the vessel with a relatively high flow velocity. We further investigated the delivery efficiency in the flowing blood environment. For both the downstream delivery and the upstream delivery, the delivery rate gradually decreased with the increase of the mean flow velocity. For downstream delivery, the delivery rate was higher than 80% with a mean flow velocity lower than 40 mm/s, and it maintained at 61.7% with an average flow velocity of 55 mm/s. Although more nanoparticles were lost in the upstream locomotion process, the delivery rate was higher than 60%, with a mean flow velocity of 40 mm/s. Precise motion control requires the real-time consistency of the real position and imaging position of the microswarm, which further influences the delivery efficiency. The comparison between the real position and imaging position of the microswarm is illustrated (fig. S33). The imaging pattern position revealed high consistency with the real position of the microswarm (in optical imaging) in a real-time manner for both stagnant and flowing blood environments. This observation gives the potential for real-time adjustment of microswarm control in response to the change in the physiological environment, thus benefitting the tracking and delivery process. The subsequent investigation in the automatic tracking of the microswarm in the vessel with both stagnant and flowing blood suggested that accurate tracking of the microswarm was feasible by LSCI (figs. S34 and S35). We created a simulation model to investigate the effect of a rotating microswarm in the bloodstream. Simulated RBCs were released from the inlet (mean flow velocity, 10 mm/s), and they contacted the microswarm and

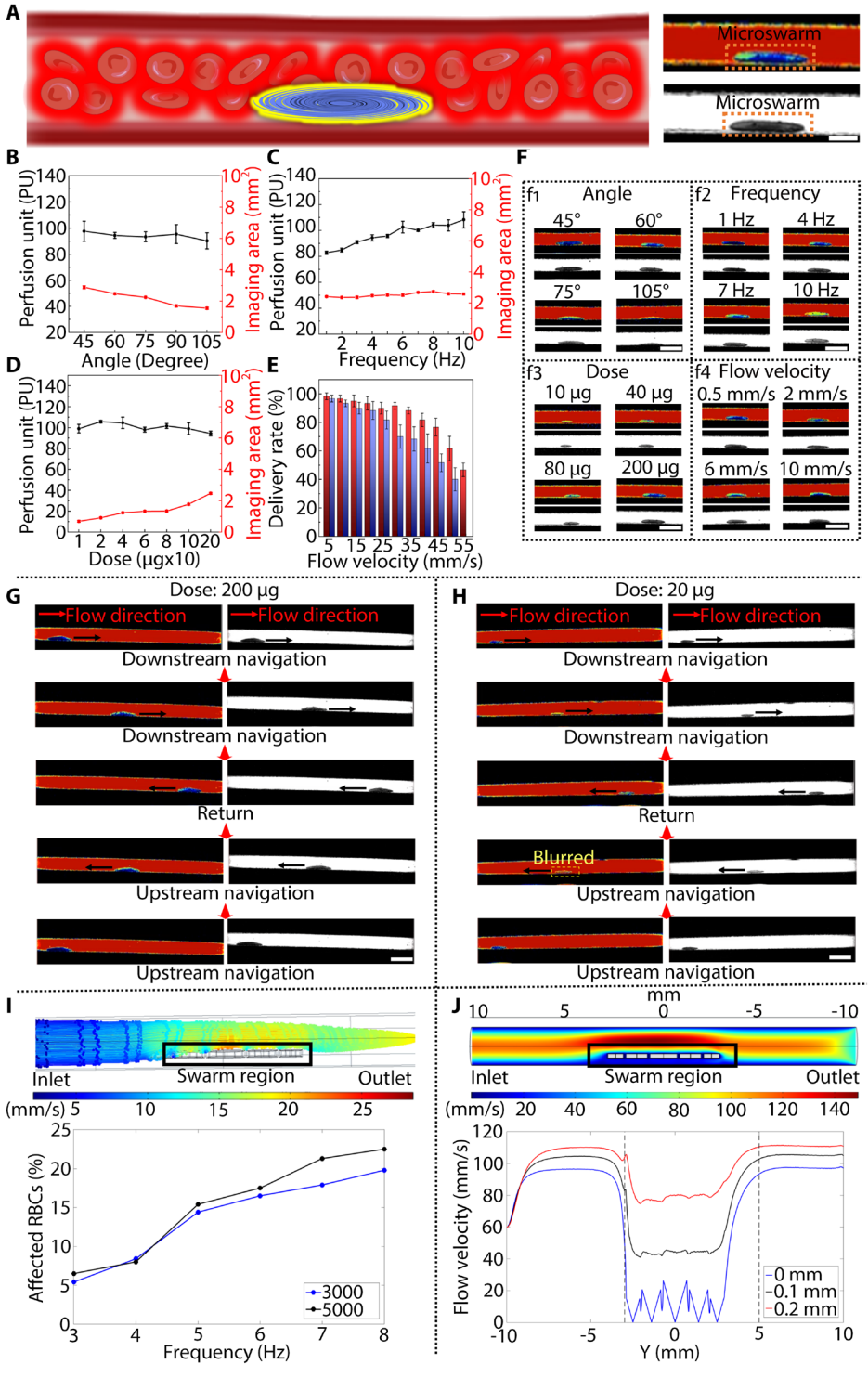

Fig. 4. Imaging and tracking of a microswarm in the vessel with flowing blood. (**A**) Schematic illustration of a microswarm in the vessel with flowing blood. The right photos show the representative pseudo-color pattern and gray pattern of a microswarm in the vessel (inner diameter, 2 mm) with dynamic bloodstream (mean flow velocity, 20 mm/s). Scale bar, 2 mm. (**B** to **D**) PU and imaging area of the microswarm change with the angle between the central axis of the magnet and the *Z* axis of the tube, input frequency, and nanoparticle dose. All statistical results are based on three experimental tests, and the error bars represent the SD of three experiments. (**E**) Delivery rates of the microswarm with different mean flow velocities ranging from 5 to 55 mm/s including downstream and upstream delivery. The red and blue bars represent the delivery rates of downstream and upstream navigation, respectively. All statistical results are based on three experimental tests, and the error bars represent the SD of three experiments. (**F**) Typical pseudo-color patterns and gray patterns of the microswarm with different input frequencies, nanoparticle doses, mean flow velocities, and angles between the central axis of the magnet and the *Z* axis of the tube. Scale bars, 5 mm. (**G** and **H**) Navigation of the microswarm (200 and 20 μg) in the vessel with flowing blood (movie S4). The black arrows refer to the locomotion direction of the microswarm. The mean flow velocity is 20 mm/s. Scale bars, 5 mm. (**I**) The simulated RBCs' trajectory and flow change when simulated RBCs pass through the microswarm. The curves show the number of the simulated RBCs that are affected by the microswarm with different input frequencies. The color bar refers to the flow velocity. (**J**) The simulation shows the stable flow distribution around the microswarm. The average flow velocity is set as 60 mm/s. The curves exhibit the flow velocity change above the microswarm with distances of 0, 1, and 2 mm. The color bar refers to the flow velocity.

changed the original motion direction because of the swarm-induced disturbance, as demonstrated by the simulated RBCs' trajectories (Fig. 4I). To quantitatively investigate the effect, input frequencies of 3 to 8 Hz were applied, and the affected simulated RBCs were calculated. A relatively high input frequency led to relatively strong hydrodynamic convection around the microswarm; thus, more simulated RBCs were affected and further changed the locomotion direction. We released 3000 and 5000 simulated RBCs to reveal the effect of the number of simulated RBCs. A numerical analysis showed that the percentage of simulated RBCs affected by the microswarm increased with the change of the input frequency in both cases, showing an enhanced interaction between the microswarm and simulated RBCs (Fig. 4I). In an environment with a relatively high blood flow (mean velocity, 60 mm/s), the microswarm resisted the blood flow and remained intact, as shown in the simulation (Fig. 4J). The simulation of the microswarm and flow distribution was also conducted at a relatively low mean flow velocity of 20 mm/s (fig. S36), where the microswarm maintained a stable state. The change of flow velocity above the microswarm with distances of 0 to 200 μm was demonstrated in Fig. 4J, and a sharp drop in flow velocity was observed close to the microswarm, which contributed to the drag resistance ability of the microswarm. The above results verified that the microswarm can be tracked and navigated in

flowing blood and that effective delivery in dynamic environments can be realized under the guidance of LSCI.

Tracking and navigation of a microswarm in the artificial blood vessel phantom

LSCI is able to provide full-field imaging of the blood vessel even with complex branching, which is critical for path planning to avoid microswarm straying (*23*). The schematic in Fig. 5A illustrates the downstream and upstream locomotion process of the microswarm in an artificial blood vessel phantom with multiple branches. An image with a 42 mm–by–42 mm size was generated by LSCI (Fig. 5B). Although the magnet generated imaging signals because of the rotating motion (Fig. 5B, b1), it did not influence the image quality of the microswarm. Here, a motion controller with 4 DOFs (degrees of freedom) was deployed to manipulate the sphere magnet and further control the locomotion of the microswarm. Figure 5B, b1 to b3, exhibits the downstream locomotion of the microswarm in the artificial blood vessel phantom, and the microswarm has a distinct imaging profile in the complex environment. After arriving at the targeted site, imaging-guided upstream navigation of the microswarm was conducted, and higher drag force could be overcome by the microswarm during the upstream locomotion. Our results verified that the microswarm was capable of moving against the relatively high blood flow (mean velocity of 20 mm/s) in the artificial blood vessel phantom, whereas real-time tracking of the microswarm was realized by LSCI (Fig. 5B, b4 to b6). The effective tracking process was conducted (Fig. 5C). The result showed that precise motion control was achieved by the rotating magnet in both downstream and upstream situations, and the mean error was 0.54 ± 0.32 and 0.62 ± 0.29 mm (three trials), respectively, indicating a reasonably accurate microswarm control and tracking strategy. Figure 5D demonstrates the tracking process of the microswarm in the artificial blood vessel phantom with real-time numerical analysis. Each tracking step was finished within 100 ms; thus, the trajectory can be treated as a real-time result with negligible time delay. Furthermore, the delivery rate after downstream and upstream locomotion was calculated, and 83.3 ± 4.71% of nanoparticles were recycled after the whole process (three trials). Although the real-time tracking and navigation of the micro/nanorobotic swarm in the vascular environment can also be achieved by US imaging (*15*, *16*, *28*), the limited acoustic window for the lumen and suboptimal ability to delineate the microswarm from the surrounding tissue environment may lead to signal loss or even imaging failure. Our demonstration shows that LSCI can provide full-field imaging of the artificial blood vessel phantom with real-time feedback, facilitating the tracking and navigation of the microswarm in complex environments.

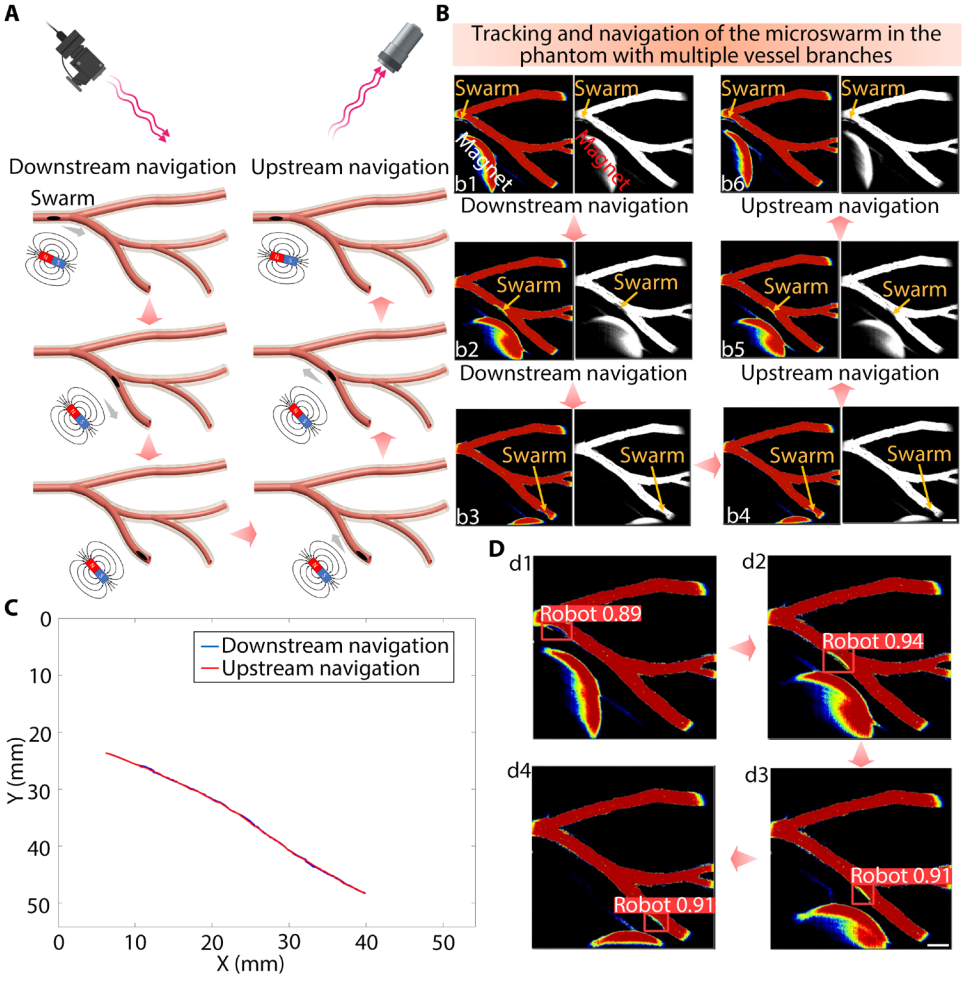

Fig. 5. Imaging and tracking of a microswarm in the artificial blood vessel phantom. (**A**) A schematic illustration of the downstream and upstream locomotion of the microswarm in the artificial blood vessel phantom with multiple vessel branches tracked by LSCI. (**B**) Tracking and navigation of the microswarm in the artificial blood vessel phantom with multiple vessel branches in real time (left, pseudo-color pattern; right, gray pattern). The nanoparticle dose is 200 μg (movie S5). (**C**) The tracking of the microswarm in the artificial blood vessel phantom with both downstream and upstream navigation. (**D**) The numerical tracking process of the microswarm with downstream locomotion in the artificial blood vessel phantom. Scale bars, 5 mm.

Real-time tracking and navigation of a microswarm ex vivo

To investigate the imaging and tracking of the microswarm in real tissue environments, we used the human placenta to demonstrate microswarm navigation over a relatively long distance, owing to the vascular architecture of the human placenta. The placenta shares features of the human brain in terms of both the predominately soft tissue composition and the complex vascular anatomy (*44*), which could be an ideal model for microswarm imaging. Figure 6A shows a photo of the human placenta with complex vasculature. The area indicated by the yellow rectangle was used as the model for investigating the tracking and navigation of the microswarm over a relatively long distance. The diameters of the model blood vessels with different

positions were measured (Fig. 6, B and C), ranging from 1.38 to 2.08 mm. The full-field imaging of the model blood vessel with branches was depicted by LSCI (Fig. 6, D and E), which enabled us to effectively track the microswarm with an extended imaging field. To control the blood flow velocity, silicone tubes were connected to the human placenta, and a peristaltic pump was used to pump whole blood into the blood vessels of the human placenta. The nanoparticles were then delivered into the blood vessel by a catheter, which was followed by the formation of a microswarm with a rotating magnetic field. Subsequently, downstream tracking and navigation were conducted, and the microswarm was able to locomote distally under the guidance of LSCI (Fig. 6D). We subsequently conducted upstream navigation, although the imaging signal was weaker than that of the microswarm in the downstream navigation process because of the high drag force induced by the blood flow. The distance traveled was approximately 80 mm after finishing the round-trip navigation. We continuously tracked and navigated the microswarm in the model blood vessel for 5 cycles, with a total navigation distance of approximately 400 mm. The fifth cycle of the navigation process is presented in Fig. 6E. Around 60% of the microswarm was recycled after the whole navigation process. The results demonstrated that the relative long-distance navigation of the microswarm can be achieved in the human placenta model under the guidance of the LSCI.

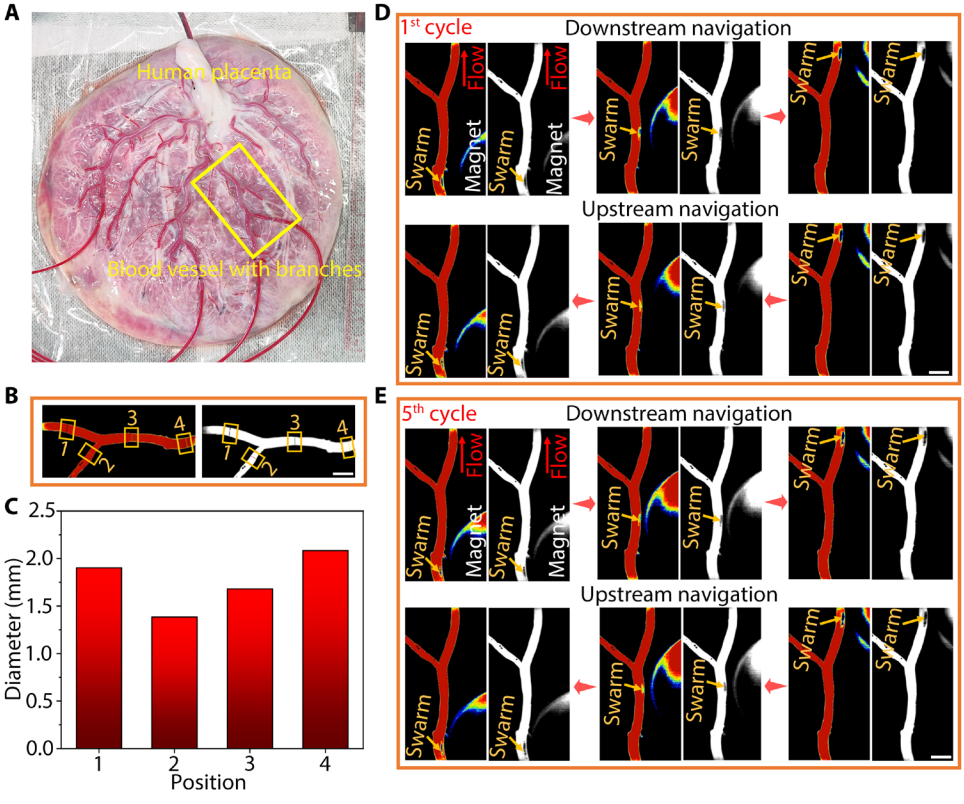

Fig. 6. Tracking and navigation of a microswarm in the human placenta. (**A**) The photo of the human placenta and a blood vessel with multiple branches circled by the yellow rectangle. (**B**) The pseudo-color pattern and gray pattern of the blood vessel with four positions for diameter measurement. (**C**) The diameter at four positions of the blood vessel was measured by LSCI. (**D**) The first cycle of tracking of the microswarm in the human placenta with both downstream and upstream navigation for a relatively long distance (total distance, around 80 mm). (**E**) The fifth cycle of tracking of the microswarm in the human placenta with both downstream and upstream navigation for a relatively long distance (total distance, around 80 mm). Scale bars, 5 mm.

Real-time tracking and navigation of a microswarm in vivo

Real-time in vivo imaging of micro/nanorobotic swarms plays a key role in effective delivery during biomedical applications. We applied LSCI to achieve real-time tracking and navigation of the microswarm in vivo. Male Sprague-Dawley rats were used in our in vivo experiment, and the rats were anesthetized before any further operation. The femoral vein of the rat was chosen as the model to verify the in vivo imaging of the microswarm. A needle was used to inject the nanoparticles via the epigastric vein of the rat with a total dosage of 200 μg. A rotating sphere magnet was placed above the femoral vein for nanoparticle gathering and swarm formation. Figure 7A depicts the whole process of imaging the microswarm in vivo, including nanoparticle injection, microswarm formation, downstream and upstream tracking, and navigation in the femoral vein guided by LSCI. The common femoral vein and epigastric vein (main branch) of the rat could be observed, which exhibited strong imaging signals induced by flowing RBCs (Fig. 7B). The sphere magnet also generated imaging signals because of its coarse surface and rotating motion, and interference could be avoided by adjusting the distance between the magnet and the blood vessel. The microswarm formation process was monitored by LSCI in real time (Fig. 7B). Before nanoparticle injection, there were no obvious imaging signals generated in the femoral vein (Fig. 7B, b1), whereas an imaging profile of collective nanoparticles appeared after the injection and gathering process (Fig. 7B, b2). Compared with nanoparticles in the gathering process, the microswarm exhibited higher imaging contrast after being completely formed in the blood vessel (Fig. 7B, b3). Subsequently, we investigated the tracking and navigation of the microswarm in the blood vessel under the guidance of LSCI. The red arrow refers to the flow direction, and the white and green arrows indicate the navigation direction in the femoral vein (Fig. 7, C and D). Controlled locomotion of the microswarm was realized with the downstream flow by adjusting the rotating magnet (Fig. 7C). During the navigation process, the microswarm was able to maintain a stable and intact state without obvious particle loss. The strong imaging contrast of the microswarm in the femoral vein facilitated precise tracking and navigation process and further enabled high delivery efficiency in vivo. After arriving at the terminal of the femoral vein, upstream locomotion of the microswarm was performed with real-time tracking and navigation, and the total locomotion distance travelled was about 16.8 mm. For upstream locomotion, the microswarm was still able to overcome the drag force induced by the bloodstream, which was achieved by our effective control strategy. Figure 7D demonstrated the imaging-guided navigation process with the

upstream flow, and the majority of the microswarm returned to the original site. The position and the moving speed of the rotating magnet could be adjusted on demand with real-time feedback of the microswarm state based on the imaging signals. Therefore, precise and effective navigation of the microswarm was achieved in the femoral vein under different flowing conditions. The quantitative result showed that 85% of the microswarm was recycled after downstream and upstream navigation in vivo. Moreover, in vivo tracking and navigation of the microswarm were conducted in the femoral vein of the rat for prolonged observation times at 5, 10, 15, 25, and 35 min and 8 s (fig. S37). The size of the microswarm gradually reduced with time, with increasing imaging signal of the separated nanoparticles as indicated by the yellow and green dashed rectangles in fig. S37D, d2 to d4. At $t = 35$ min and 8 s, imaging signals of the microswarm vanished, indicating that the microswarm disappeared in the presence of high blood flow. Our results confirmed the feasibility of LSCI to track microswarm status for a duration of up to 35 min in the absence of ionizing radiation. The proposed strategy, therefore, offers great potential in biomedical applications as a radiation-free, real-time, and prolonged in vivo tracking method of a microrobotic swarm with high delivery efficiency.

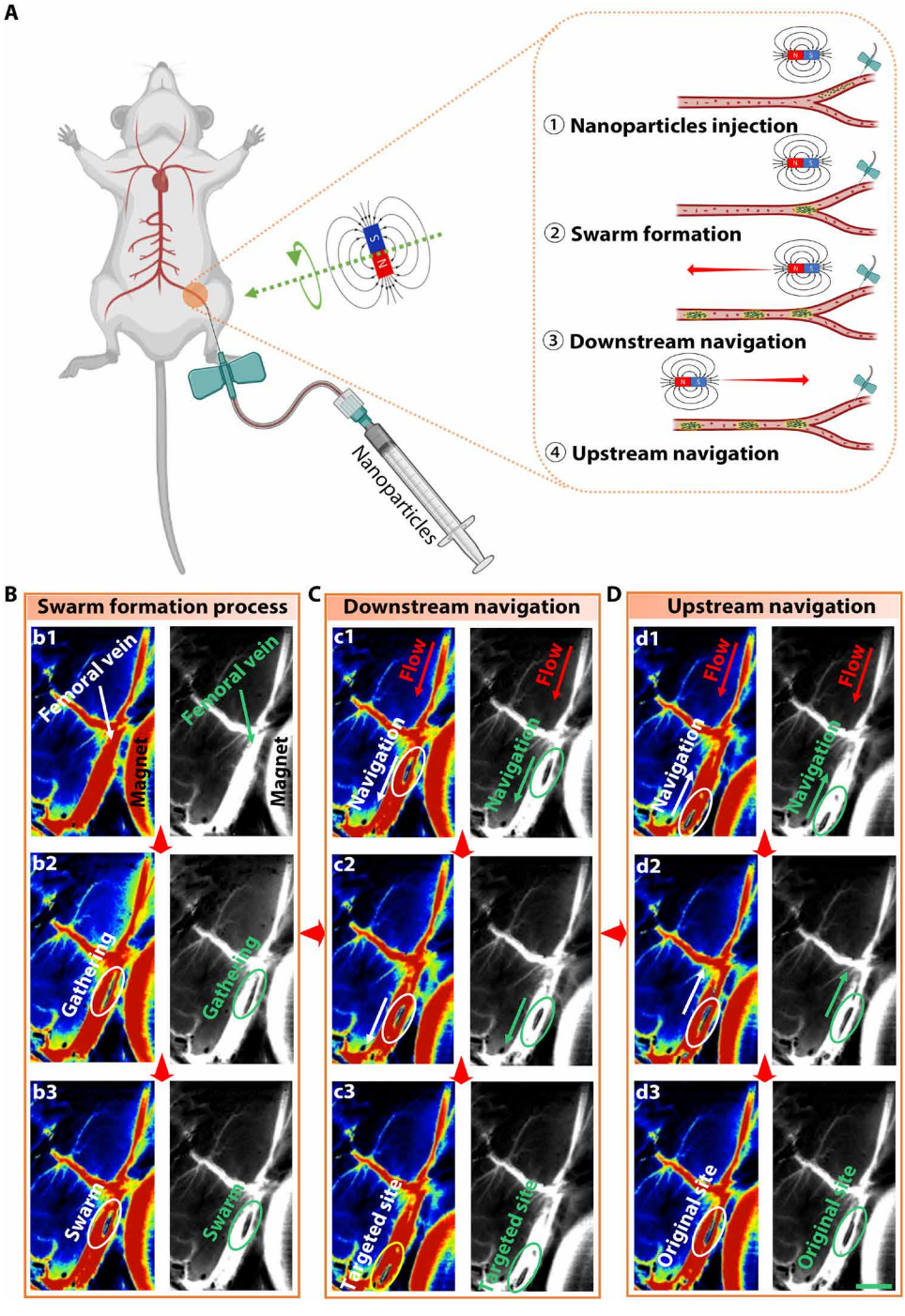

Fig. 7. Real-time tracking and navigation of a microswarm in vivo. (**A**) Tracking and navigation of a microswarm in the femoral vein of the rat guided by LSCI. (**B**) Photographs show the microswarm formation process inside the femoral vein of the rat. The sphere magnet was placed on the right side of the blood vessel to generate a rotating magnetic field (movie S6). (**C** and **D**) Downstream and upstream navigation was achieved with real-time tracking by LSCI (nanoparticle dose, 200 μg). The red arrows refer to the flow direction; white and green arrows denote the navigation direction (movie S6). Scale bar, 5 mm (B to D).

DISCUSSION

Precise tracking and navigation improve the delivery efficiency of micro/nanorobots and thus are essential for imaging-guided safe and efficacious biomedical applications (*45*–*48*). Although challenging, these goals may be achieved by accurate real-time imaging guidance under biological environments, especially in the endovascular system. To date, many imaging modalities have been evaluated for detecting and tracking micro/nanorobots, aiming at improved targeting ability and delivery efficiency (*11*). Nonetheless, owing to the shortcomings in radiation hazard, temporal resolution, signal-to-noise ratio, and penetration depth among the common imaging modalities discussed above, there is an unmet need for a real-time, high-resolution, and large-area imaging method of micro/nanorobots. Such an ideal dynamic imaging assessment benefits the fundamental investigation of the micro/nanorobot-environment interactions and may further facilitate research in endovascular intervention, such as cancer therapy and thrombolysis (*49*–*52*). Our present study that used LSCI unlocked the opportunity for high-quality and real-time feedback to aid efficient tracking and navigation of a magnetic swarm in biological vascular systems.

Investigation of the microswarm-environment interactions strengthens the fundamental understanding of collective behaviors and facilitates the targeted delivery process. In our strategy, both imaging signal intensity and pattern-environment interactions were quantitatively explored by analyzing the PU change (*43*, *53*). Fe_3O_4@SiO_2 nanoparticles are tiny building blocks that can form a microswarm by applying a rotating magnetic field generated by a sphere magnet (*28*, *54*, *55*). The induced microswarm and its interactions with the environment, including the bloodstream and vessel wall, were captured and quantified by LSCI. Through images and parameters generated by LSCI, we were able to demonstrate that the collective behavior of microswarm enabled the generation of images with enhanced contrast compared with spread nanoparticles without a rotating magnetic field (*22*, *28*), and the different pattern-environment interactions when exposed to different environmental variables, such as input frequency, flat surface, and vessels with different blood flow velocities. For example, the PU value was controlled in a range of 94.5 to 184.7 by adjusting input frequency and could be assessed in a real-time manner with an imaging field of around 7 mm^2 for input frequencies larger than 3 Hz in a vessel with stagnant blood (Fig. 3D). Therefore, the hydrodynamic convection of the microswarm can be fine-tuned to aid drug delivery in an optimized manner under pathological conditions, such as blood vessel occlusions (*36*, *37*). Under models with flowing blood, we found that the microswarm exhibited a smaller image but could be improved by reducing the capture angle from 105° to 45° as illustrated in Fig. 4B (from 1.55 to 2.89 mm^2). Furthermore, the drag force under a blood flow was reduced by navigating the microswarm close to the vessel wall, thus permitting downstream and upstream locomotion ability. The delivery efficiency of the microswarm was quantified as over 90% downstream and 81% upstream with a mean flow velocity of 25 mm/s (Fig. 4E), demonstrating a high delivery efficiency under LSCI.

Although conventional optical-based imaging methods, such as optical coherence tomography and fluorescence imaging, are safe and inexpensive with high spatial-temporal resolutions (*14*, *56*), the low penetration depth below 1 mm in biological environments limits their assessment in deeper subsurfaces (*57*, *58*). On the contrary, LSCI was able to capture the imaging signal generated by the interaction between the microswarm and RBCs with a blood depth of 3.5 mm (Fig. 2I). Although methods to improve the imaging depth and resolution of conventional optical imaging tools, such as incorporation of contrast agents (metal Au) or labels (fluorescence dyes) into micro/nanorobots, have been described, they require complex modification processes and may not be able to resolve issues such as limited signal intensity, photobleaching, and short shelf lives (*17*, *18*). Our proposed method by LSCI, on the other hand, did not require modifications of the microswarm and was still able to conduct real-time imaging and tracking of the microswarm in various blood environments (Figs. 3I and 4G). Even at a low dose (20 μg), the microswarm maintained a relatively strong imaging signal intensity in the flowing blood model (Fig. 4H). The proposed strategy achieves imaging and tracking of the microswarm in blood environments without chemical modifications of contrast agents or labels, which expands the capability of imaging-guided targeted delivery for biomedical applications.

Besides optic-based methods, US imaging has also been used for imaging and tracking of the micro/nanorobots in the vascular environment, with the advantages of deep tissue penetration and real-time feedback (*15*, *28*, *59*). However, probe manipulation is frequently required because of the limited imaging window, especially for tracing the locomotion of micro/nanorobots over a long distance. Probe manipulation may also run into risks of signal loss or even imaging failure. Because of the limited acoustic window, US imaging is also not able to depict complex vascular anatomies in a single image and therefore needs complex manipulations for monitoring and on-demand control of the micro/nanorobots (*11*). In our work, an artificial blood vessel phantom and a placenta with complex vascular branching were used to validate the capability of LSCI to image the microswarm in complex environments. Full-field images were obtained without adjusting the detector, which, at the same time, guided the microswarm locomotion to the target site (Figs. 5B and 6D). Precise motion control was achieved in both downstream and upstream navigation, with a mean error of 0.54 ± 0.32 and 0.62 ± 0.29 mm (7.7 and 8.9% body length), respectively, demonstrating that control and tracking of microswarm are effectively guided by LSCI.

In vivo imaging of micro/nanorobots under biological environments is challenging (*60*–*63*) with the following key issues: Drag force induced by the bloodstream may hinder the controllable movability of the micro/nanorobots; there is a lack of reliable real-time feedback of the state of micro/nanorobots in the real physiological environment to allow timely adjustment of micro/nanorobot control; long-distance navigation and tracking of micro/nanorobot are limited by the lack of large-area imaging that instantly depicts complex vascular architectures. Here, we reported real-time tracking and navigation of the microswarm in a rat model (Fig. 7B). With real-time supervision using LSCI, the microswarm was formed without detectable loss of nanoparticles through navigation close to the vessel wall in an attempt to minimize the drag force under both downstream and upstream situations (Fig. 7, C and D). The full-field imaging by LSCI also enabled navigation of the microswarm into vascular tributaries of a rat femoral vein over a distance of 16.8 mm without probe adjustment. The targeting ability of the microswarm was also enhanced, leading to high delivery efficiency. A high proportion (>85%) of the microswarm was recycled after the navigation process under LSCI guidance. Our observation suggested that LSCI can monitor blood flow in real time and has the potential to create micro/nanorobotic platforms that guide experiments in endovascular interventions, such as thrombus removal and revascularization of vessel stenosis.

Although LSCI represents a promising tool in our experiments based on artificial blood vessel phantom, placental, and rat models, it should be noted that the application of LSCI on larger animals and humans could be challenging. First, vessel pathologies in humans usually occur in deep vascular systems, such as deep venous thrombosis and intracranial arterial occlusions. These systems are usually protected by thick tissues or bones and are not readily penetrated by LSCI from the skin surface (*64*, *65*). However, LSCI may still play a role in superficial blood vessels, such as superficial veins of the upper limbs, lower limbs, and ears of large animals. Surgical exposure of the target site may be necessary to study microswarm behaviors within deep vascular systems in large animals. Second, although we were able to demonstrate tracking of the microswarm over a distance by LSCI in placental and rat models, tracking microswarm in large animals may require a more extensive image field for continuous guidance. Alternatively, the laser probe can be coupled with the robotic control module, thus enabling on-demand control

of the laser position to track the long-range delivery of the microswarm (*59*). Third, because of the body length of large animals, endovascular catheterization of target vessels from distant vascular access may be necessary to optimize the delivery of the microswarm (*66*, *67*). More precise navigation of microswarm can then follow, especially to small-caliber and/or tortuous blood vessels that current endovascular catheters are unable to reach. We believe that the integration of the long-distance delivery ability of catheter and LSCI-guided microswarm delivery strategy in the vascular environment can potentially benefit the long-range intervention process and ensure high delivery efficiency in large bodies. Last, LSCI imaging is highly dependent on the used experimental parameters, such as magnetic field frequency, laser angle, and blood environments. Therefore, it is important to optimize the parameters to suit the imaging of the microswarm under specific experimental conditions. Because LSCI provides real-time imaging of the microswarm and the positions of the real image and the LSCI image have more parameter-independent correspondence, parameter adjustment in response to changing experimental conditions could be performed in a real-time manner to optimize its tracking and delivery process.

In summary, our proposed method of real-time tracking and navigation of the magnetic microswarm by LSCI enables visualization and quantitative assessment of the microswarm under in vitro and in vivo vascular environments. The microswarm-environment interactions were quantitatively accessed in different environments, and high-efficiency delivery was realized with a maximal mean flow velocity of 55 mm/s. Moreover, under the guidance of LSCI, a high delivery efficiency of the microswarm in the vessel was achieved even with blood flow in vivo. Our work presents a promising strategy for tracking and navigation of the micro/nanorobotic swarm in vascular systems that may aid biomedical applications that require accurate target delivery with high efficiency.

MATERIALS AND METHODS

Materials

$FeCl_3{\cdot}6H_2O$ [iron (III) chloride hexahydrate], tannic acid (TA), sodium citrate (SC), gold chloride trihydrate ($HAuCl_4{\cdot}3H_2O$), citric acid monohydrate ($C_6H_8O_7{\cdot}H_2O$), potassium carbonate (K_2CO_3), hexadecyltrimethylammonium chloride (CTAC), tetraethyl orthosilicate (TEOS), 1-octadecene, and ethylene glycol (EG) were obtained from Aladdin Chemical Co. Ltd. Polyethylene glycol [PEG; M_w (weight-average molecular weight) = 2000], $C_2H_3NaO_2{\cdot}3H_2O$ (sodium acetate trihydrate), and triethanolamine (TEA) were purchased from Sigma-Aldrich. Tris was purchased from Acros Organics. All chemical agents were used without any further purification.

Synthesis of Fe_3O_4@SiO_2 nanoparticles

The synthesis of Fe_3O_4 nanoparticles was based on a previous report (*68*). Briefly, 1.35 g of $FeCl_3{\cdot}6H_2O$ was added to 40 ml of EG followed by mechanical stirring. After completely dissolving, sodium acetate trihydrate (3.6 g) and PEG (1.0 g) were added, and then continuous mechanical stirring was performed overnight. Then, the mixture solution was sealed in a Teflon autoclave and heated at 200°C for 10 hours. Subsequently, the autoclave cooled to room temperature, and the black product was collected by a permanent magnet and washed with ethanol and deionized (DI) water three times. Last, the Fe_3O_4 nanoparticles were stored in DI water for further use.

Fe_3O_4@SiO_2 nanoparticles were prepared according to previous literature with some modifications (*69*). Briefly, 100 mg of Fe_3O_4 nanoparticles and 6 g of CTAC were dispersed in a round-bottom flask with 120 ml of water and then ultrasonicated with mechanical stirring at a constant temperature of 60°C. Next, 320 μl of TEA was added to the flask. After that, 40 ml of 1-octadecene solution mixed with 10% (v/v) TEOS was added into the aqueous phase three times with time intervals of 10 min and treated for 15 hours. Last, the black products were obtained by using a magnet and washed three times with DI water and ethanol, respectively. Fe_3O_4@SiO_2 nanoparticles were stored in phosphate-buffered saline at a concentration of 2 mg/ml.

Synthesis of Fe_3O_4@PDA nanoparticles

Fe_3O_4@PDA nanoparticles were prepared on the basis of the previous report (*68*). First, 0.12 g of tris was added to a beaker with 100 ml of DI water. After dissolving, the pH value was adjusted to 8.5 using HCl (1 M). Next, the buffer was added into a round-bottom flask, and 100 mg of Fe_3O_4 nanoparticles was added. Then, the mixture was stirred and sonicated for 30 min to fully disperse Fe_3O_4 nanoparticles. Subsequently, 0.02 g of dopamine hydrochloride was added to the mixture with continuous stirring and sonication for 5 hours. Last, the black product was collected using a permanent magnet and washed with ethanol and DI water three times. The Fe_3O_4@PDA nanoparticles were dispersed in DI water for further use.

Synthesis of Fe_3O_4@PDA@Au nanoparticles

Au seeds were prepared on the basis of the previous report (*70*). Briefly, 0.1 ml of TA (2.5 mM) and 1 ml of K_2CO_3 (150 mM) were added into a round-bottom flask with 150 ml of solution of SC (2.2 mM), and then 1 ml of $HAuCl_4$ (25 mM) was slowly added at 70°C followed by 5 min of reaction. After that, the Au seed solution was obtained. Then, the surface charge of Fe_3O_4@PDA was adjusted to positive. Specifically, 0.158 g of $C_6H_8O_7{\cdot}H_2O$ was added to 50 ml of DI water. After dissolving, the pH value of the solution was turned to 2.0 by 1 M HCl to form the buffer. Subsequently, 10 mg of Fe_3O_4@PDA nanoparticles was added into the buffer with mechanical stirring and sonication for 15 min. Then, the Au seed solution was poured into the buffer solution with 10 mg of Fe_3O_4@PDA nanoparticles, and the Fe_3O_4@PDA@Au nanoparticles were collected after 30 min and further stored in DI water for further use.

Simulations of microswarm-induced flow and simulated RBCs

All simulations were conducted in COMSOL Multiphysics. Simulation of the RBCs' motion in stagnant blood around a rotating microswarm was designed in a three-dimensional Rotating Machinery module (Figs. 2B and 3B). The fluid density and viscosity were set as 1.04×10^3 kg/m^3 and 4.5×10^{-3} Pa·s, respectively, to simulate blood environment. Simulated RBCs (total of 3000 microparticles, 6 μm in diameter and 1.08×10^3 kg/m^3 in density) were released after the rotating microswarm reached an equilibrium state, and the RBCs' motion was governed by the drag force from the induced fluid flow. Simulations in the bloodstream were conducted by adding the inlet and outlet (Fig. 4, I and J). The simulated RBCs were released after the rotating microswarm reached an equilibrium state (Fig. 4I). If the microparticle's *X*-*Z* position changed (bloodstream along the *Y* axis) after reaching the outlet, then it was defined as affected simulated RBCs; thus, the ratio of

affected simulated RBCs could be calculated. The microswarm-distorted flow profile in Fig. 4J was acquired in the simulation. The data points were replotted in MATLAB.

Formation of a microswarm on the flat surface

To form a microswarm on the flat surface, a plate tank with a diameter of 35 mm was used in our experiment. Fresh pig blood was poured into the tank with various volumes to obtain different blood depths, and 0.96 ml of pig blood yielded a depth of 1 mm. Fe_3O_4@SiO_2 nanoparticles (20 μl) were added into the tank, and a sphere magnet with a diameter of 20 mm was used to generate the rotating magnetic field. Unless otherwise stated, the experimental parameters were set as follows: input frequency, 4 Hz; nanoparticle dose, 40 μg; blood depth, 2 mm; distance between the magnet tip and the swarm plane, 10 mm. The tank was placed under the LSCI for imaging of the microswarm, and the working distance between the tank and LSCI was kept at 130 mm. The PU was obtained by measuring the whole imaging pattern, representing the average value of the whole pattern. All statistical results are based on three experimental tests, and Fig. 2 (D to G) is plotted with SD.

Imaging and tracking of the microswarm in the vessel

A silicone tube with an inner diameter of 2 mm was used to investigate the imaging and tracking of the microswarm in the vessel. The inner diameter of the tube was set as 2 mm unless stated otherwise. The tube was connected to a peristaltic pump to control the mean flow velocity, and the working distance of the LSCI system was kept at 130 mm. For stagnant blood, 100 μl of Fe_3O_4@SiO_2 nanoparticles was injected into the tube filled with blood, and a rotating magnetic field (magnetic field strength, 64.9 mT; input frequency, 4 Hz) was applied to form the microswarm. The rotating magnet was settled on a motion controller with 4 DOFs; thus, the locomotion of the microswarm was achieved by moving the rotating magnet. The position of the microswarm in the tube could be adjusted by the angle between the central axis of the magnet and the *Z* axis of the tube, as described in fig. S14. Unless otherwise stated, the experimental parameters were set as follows: input frequency, 4 Hz; nanoparticle dose, 200 μg; distance between the magnet tip and the swarm plane, 5 mm; angle between the central axis of the magnet and the *Z* axis of the tube, 60°. To avoid interference, the distance was set as 10 mm when varying the angle. For flowing blood, 100 μl of Fe_3O_4@SiO_2 nanoparticles was injected into the tube filled with blood, and the mean flow velocity was controlled by the rotation speed of the peristaltic pump. To resist the high flow, the distance was set as 5 mm with a magnetic field strength of 121.5 mT. Unless otherwise stated, the experimental parameters were set as follows: mean flow velocity, 20 mm/s; input frequency, 4 Hz; nanoparticle dose, 200 μg; distance between the magnet tip and the swarm plane, 5 mm; angle between the central axis of the magnet and the *Z* axis of the tube, 60°. For calculation of the delivery rate, 0.2 mg of Fe_3O_4@SiO_2 nanoparticles was used for each trial, and the microswarm locomoted (downstream or upstream) for a distance of 40 mm with the guidance of the LSCI. Then, the residual Fe_3O_4@SiO_2 nanoparticles were recollected by a magnet and dried in an oven. Last, the residual Fe_3O_4@SiO_2 nanoparticles were weighted for calculation. The delivery rate was calculated by the equation

$$w_r / w_0 \times 100\% \quad (5)$$

where w_r and w_0 refer to the recycled weight and original weight, respectively. All statistical results are based on three experimental tests, and Fig. 3 (C to F) is plotted with SD.

Tracking and navigation of a microswarm in the artificial blood vessel phantom

The artificial blood vessel phantom with multiple branches was purchased from WeNext Technology Co. Ltd., which was printed with transparent resin. The artificial blood vessel phantom was connected with a peristaltic pump to control the mean flow velocity (20 mm/s in the main branch). Then, 100 μl of Fe_3O_4@SiO_2 nanoparticles was injected into the artificial blood vessel phantom from the inlet. The working distance of the LSCI system was fixed at 130 mm. The rotating magnet (input frequency, 4 Hz; distance between the magnet tip and the swarm plane, 5 mm) was applied with an angle of 45° (the angle between the central axis of the magnet and the *Z* axis of the tube), and tracking and navigation of the microswarm in the artificial blood vessel phantom were conducted. Unless otherwise stated, the distance was defined as the distance between the tip of the magnet and the plane of the microswarm. After downstream and upstream locomotion, the microswarm was harvested by using a magnet, followed by drying and weighing. The delivery rate was calculated by Eq. 5. All statistical results were based on three experimental tests, and Fig. 4 (B to E) is plotted with SD.

Imaging and navigation of a microswarm ex vivo

The human placenta was collected from the Prince of Wales Hospital, which was approved and overseen by the Joint Chinese University of Hong Kong (CUHK)–New Territories East Cluster Clinical Research Ethics Committee (ref. no. 2020.384). The human placenta was donated by a pregnant woman who received a cesarean section at Prince of Wales Hospital, collaborating with the Department of Obstetrics and Gynaecology (CUHK). A written informed consent was provided by the enrolled patient. Eligible patients were healthy pregnant women at 20 to 45 years of age of any ethnic origin giving birth with cesarean sections after 37 to 42 weeks of gestation; singleton pregnancy; healthy as determined by treating physicians, laboratory results (blood routine examination, urine routine examination, and antigen and antibody detection), physical examination, and medical history; and the ability to give voluntary, written, informed consent to participate in the study. Exclusion criteria were abnormal prenatal development, hypercholesterolemia, family history of stroke or vascular diseases, diabetes, gestational diabetes, and cancer. After collection, the placenta was washed with saline, and the blood inside of the blood vessels was removed to prevent occlusion. The fetal membrane was removed and cut into small pieces with a length of around 50 mm and a width of around 40 mm. The average thickness of the fetal membrane was measured with 12 pieces by the microscope. Different layers of the fetal membrane were covered on the tank or the tube for imaging of the microswarm offering the mimicking tissue environment. The experimental parameters are set as follows (flat surface): input frequency, 4 Hz; nanoparticle dose, 40 μg; distance between the magnet tip and the swarm plane, 10 mm; blood depth, 2 mm. The experimental parameters are set as follows (tube with stagnant blood): input frequency, 4 Hz; nanoparticle dose, 200 μg; distance between the magnet tip and the swarm plane, 5 mm; angle between the central axis of the

magnet and the *Z* axis of the tube, 60°. The experimental parameters are set as follows (tube with flowing blood): input frequency, 4 Hz; nanoparticle dose, 200 μg; distance between the magnet tip and the swarm plane, 5 mm; the angle between the central axis of the magnet and the *Z* axis of the tube, 60°; mean flow velocity: 20 mm/s.

For tracking and navigation of the microswarm in the placenta, the human placenta was connected with a peristaltic pump by silicon tubes to control the mean flow velocity (20 mm/s in the main branch). Fe_3O_4@SiO_2 nanoparticles (200 μg) were deployed into the catheter and then released before forming the microswarm. The working distance of the LSCI system was fixed at 130 mm, and the rotating magnet (input frequency, 4 Hz; distance between the magnet tip and the swarm plane, 5 mm) was applied with an angle of 60° (the angle between the central axis of the magnet and the *Z* axis of the blood vessel). The tracking and navigation of the microswarm in the placenta were conducted for five circles. Unless otherwise stated, the distance was defined as the distance between the tip of the magnet and the plane of the microswarm. After downstream and upstream locomotion, the microswarm was harvested by using a magnet, followed by drying and weighing. The delivery rate was calculated by Eq. 5. All statistical results are based on three experimental tests.

Tracking and navigation of a microswarm in vivo

The animal experiments were authorized by the Animal Experimentation Ethics Committee (no. 20-148-CRF) in the CUHK. Male Sprague-Dawley rats weighing 300 to 350 g (8 to 12 weeks) were provided by the laboratory animal services center of the CUHK without genetic modification. Before any operation, the rats were anesthetized via the intraperitoneal injection of xylazine (10 mg/kg of body weight) and ketamine (80 mg/kg of body weight) mixed with saline solution. The fur was cleaned by using an electric razor; then, the femoral vein was exposed by surgery. Subsequently, the rat was placed under the LSCI with a working distance of 130 mm. After that, an indwelling needle was punctured into the epigastric vein of the rat after the nanoparticles injection process (200 μg). A sphere magnet with a diameter of 20 mm and an input frequency of 4 Hz was applied for control and manipulation of the microswarm. The nanoparticle gathering and swarm formation process were monitored by LSCI in real time. After the microswarm formation, the downstream and upstream navigation of the microswarm in the femoral vein was conducted with real-time feedback of imaging signals. We stopped the blood flow by clamping the ends of the vessel with two hemostats after finishing the procedure; then, nanoparticles were collected, followed by drying, weighting, and calculation. Last, the rat was sacrificed. The delivery rate was calculated by Eq. 5. The in vivo experiments were repeated three times.

Characterization and measurements

TEM images were obtained using the JEOL model JEM-2011 system. The microswarm imaging was conducted by the laser speckle blood flow imaging system (RWD RFLSI III). The magnetic field strength was obtained by a gaussmeter (HT201). Reflectivity was measured by the UV-3600 ultraviolet–visible–near infrared (UV-VIS-NIR) spectrophotometer (SHIMADZU). The magnetic properties of nanoparticles were obtained using a PPMS Model 6000 Quantum Design VSM.

Supplementary Materials

This PDF file includes:

Figs. S1 to S37
Tables S1 and S2
Legends for movies S1 to S6
Reference (*71*–*75*)

Other Supplementary Material for this manuscript includes the following:

Movies S1 to S6

REFERENCES AND NOTES

1. B. Wang, K. Kostarelos, B. J. Nelson, L. Zhang, Trends in micro–/nanorobotics: Materials development, actuation, localization, and system integration for biomedical applications. *Adv. Mater.* **33**, e2002047 (2021).
2. H. Ceylan, I. C. Yasa, U. Kilic, W. Hu, M. Sitti, Translational prospects of untethered medical microrobots. *Prog. Biomed. Eng.* **1**, 012002 (2019).
3. J. Yoo, S. Tang, W. Gao, Micro- and nanorobots for biomedical applications in the brain. *Nat. Rev. Bioeng.* **1**, 308–310 (2023).
4. W. Chen, H. Zhou, B. Zhang, Q. Cao, B. Wang, X. Ma, Recent progress of micro/nanorobots for cell delivery and manipulation. *Adv. Funct. Mater.* **32**, 2110625 (2022).
5. J. Li, B. Esteban-Fernández de Ávila, W. Gao, L. Zhang, J. Wang, Micro/nanorobots for biomedicine: Delivery, surgery, sensing, and detoxification. *Sci. Robot.* **2**, eaam6431 (2017).
6. Z. Wu, Y. Chen, D. Mukasa, O. S. Pak, W. Gao, Medical micro/nanorobots in complex media. *Chem. Soc. Rev.* **49**, 8088–8112 (2020).
7. Y. Dong, L. Wang, V. Iacovacci, X. Wang, L. Zhang, B. J. Nelson, Magnetic helical micro–/nanomachines: Recent progress and perspective. *Matter* **5**, 77–109 (2022).
8. C. K. Schmidt, M. Medina-Sánchez, R. J. Edmondson, O. G. Schmidt, Engineering microrobots for targeted cancer therapies from a medical perspective. *Nat. Commun.* **11**, 5618 (2020).
9. C. Gao, Y. Wang, Z. Ye, Z. Lin, X. Ma, Q. He, Biomedical micro–/nanomotors: From overcoming biological barriers to in vivo imaging. *Adv. Mater.* **33**, e2000512 (2021).
10. Q. Wang, L. Zhang, External power-driven microrobotic swarm: From fundamental understanding to imaging-guided delivery. *ACS Nano* **15**, 149–174 (2021).
11. A. Aziz, S. Pane, V. Iacovacci, N. Koukourakis, J. Czarske, A. Menciassi, M. Medina-Sánchez, O. G. Schmidt, Medical imaging of microrobots: Toward in vivo applications. *ACS Nano* **14**, 10865–10893 (2020).
12. S. Pané, J. Puigmartí-Luis, C. Bergeles, X.-Z. Chen, E. Pellicer, J. Sort, V. Počepcová, A. Ferreira, B. J. Nelson, Imaging technologies for biomedical micro- and nanoswimmers. *Adv. Mater. Technol.* **4**, 1800575 (2019).
13. G. Go, A. Yoo, K. T. Nguyen, M. Nan, B. A. Darmawan, S. Zheng, B. Kang, C.-S. Kim, D. Bang, S. Lee, K.-P. Kim, S. S. Kang, K. M. Shim, S. E. Kim, S. Bang, D.-H. Kim, J.-O. Park, E. Choi, Multifunctional microrobot with real-time visualization and magnetic resonance imaging for chemoembolization therapy of liver cancer. *Sci. Adv.* **8**, eabq8545 (2022).
14. X. Yan, Q. Zhou, M. Vincent, Y. Deng, J. Yu, J. Xu, T. Xu, T. Tang, L. Bian, Y.-X. J. Wang, K. Kostarelos, L. Zhang, Multifunctional biohybrid magnetite microrobots for imaging-guided therapy. *Sci. Robot.* **2**, eaaq1155 (2017).
15. J. Yu, D. Jin, K.-F. Chan, Q. Wang, K. Yuan, L. Zhang, Active generation and magnetic actuation of microrobotic swarms in bio-fluids. *Nat. Commun.* **10**, 5631 (2019).
16. L. Wang, J. Wang, J. Hao, Z. Dong, J. Wu, G. Shen, T. Ying, L. Feng, X. Cai, Z. Liu, Y. Zheng, Guiding drug through interrupted bloodstream for potentiated thrombolysis by C-shaped magnetic actuation system in vivo. *Adv. Mater.* **33**, e2105351 (2021).
17. Y. Zhang, L. Zhang, L. Yang, C. I. Vong, K. F. Chan, W. K. K. Wu, T. N. Y. Kwong, N. W. S. Lo, M. Ip, S. H. Wong, J. J. Y. Sung, P. W. Y. Chiu, L. Zhang, Real-time tracking of fluorescent magnetic spore-based microrobots for remote detection of *C. diff* toxins. *Sci. Adv.* **5**, eaau9650 (2019).
18. A. Servant, F. Qiu, M. Mazza, K. Kostarelos, B. J. Nelson, Controlled in vivo swimming of a swarm of bacteria-like microrobotic flagella. *Adv. Mater.* **27**, 2981–2988 (2015).
19. Z. Xu, M. Chen, H. Lee, S.-P. Feng, J. Y. Park, S. Lee, J. T. Kim, X-ray-powered micromotors. *ACS Appl. Mater. Inter.* **11**, 15727–15732 (2019).
20. R. Tan, X. Yang, H. Lu, L. Yang, T. Zhang, J. Miao, Y. Feng, Y. Shen, Nanofiber-based biodegradable millirobot with controllable anchoring and adaptive stepwise release functions. *Matter* **5**, 1277–1295 (2022).
21. D. Vilela, U. Cossío, J. Parmar, A. M. Martínez-Villacorta, V. Gómez-Vallejo, J. Llop, S. Sánchez, Medical imaging for the tracking of micromotors. *ACS Nano* **12**, 1220–1227 (2018).
22. M. Sun, K. F. Chan, Z. Zhang, L. Wang, Q. Wang, S. Yang, S. M. Chan, P. W. Y. Chiu, J. J. Y. Sung, L. Zhang, Magnetic microswarm and fluoroscopy-guided platform for biofilm eradication in biliary stents. *Adv. Mater.* **34**, e2201888 (2022).
23. L. Yang, J. Jiang, X. Gao, Q. Wang, Q. Dou, L. Zhang, Autonomous environment-adaptive microrobot swarm navigation enabled by deep learning-based real-time distribution planning. *Nat. Mach. Intell.* **4**, 480–493 (2022).

24. V. Iacovacci, A. Blanc, H. Huang, L. Ricotti, R. Schibli, A. Menciassi, M. Behe, S. Pané, B. J. Nelson, High-resolution SPECT imaging of stimuli-responsive soft microrobots. *Small* **15**, e1900709 (2019).
25. Z. Wu, L. Li, Y. Yang, P. Hu, Y. Li, S.-Y. Yang, L. V. Wang, W. Gao, A microrobotic system guided by photoacoustic computed tomography for targeted navigation in intestines in vivo. *Sci. Robot.* **4**, eaax0613 (2019).
26. L. Xie, X. Pang, X. Yan, Q. Dai, H. Lin, J. Ye, Y. Cheng, Q. Zhao, X. Ma, X. Zhang, G. Liu, X. Chen, Photoacoustic imaging-trackable magnetic microswimmers for pathogenic bacterial infection treatment. *ACS Nano* **14**, 2880–2893 (2020).
27. P. Wrede, O. Degtyaruk, S. K. Kalva, X. L. Deán-Ben, U. Bozuyuk, A. Aghakhani, B. Akolpoglu, M. Sitti, D. Razansky, Real-time 3D optoacoustic tracking of cell-sized magnetic microrobots circulating in the mouse brain vasculature. *Sci. Adv.* **8**, eabm9132 (2022).
28. Q. Wang, K. F. Chan, K. Schweizer, X. Du, D. Jin, S. C. H. Yu, B. J. Nelson, L. Zhang, Ultrasound doppler-guided real-time navigation of a magnetic microswarm for active endovascular delivery. *Sci. Adv.* **7**, eabe5914 (2021).
29. H. Joh, D. E. Fan, Materials and schemes of multimodal reconfigurable micro/nanomachines and robots: Review and perspective. *Adv. Mater.* **33**, e2101965 (2021).
30. G.-Z. Yang, J. Bellingham, P. E. Dupont, P. Fischer, L. Floridi, R. Full, N. Jacobstein, V. Kumar, M. McNutt, R. Merrifield, B. J. Nelson, B. Scassellati, M. Taddeo, R. Taylor, M. Veloso, Z. L. Wang, R. Wood, The grand challenges of *Science Robotics*. *Sci. Robot.* **3**, eaar7650 (2018).
31. L. Yang, J. Yu, S. Yang, B. Wang, B. J. Nelson, L. Zhang, A survey on swarm microrobotics. *IEEE Trans. Robot.* **38**, 1531–1551 (2022).
32. D. Jin, L. Zhang, Collective Behaviors of magnetic active matter: Recent progress toward reconfigurable, adaptive, and multifunctional swarming micro/nanorobots. *Acc. Chem. Res.* **55**, 98–109 (2022).
33. X. Du, J. Yu, D. Jin, P. W. Y. Chiu, L. Zhang, Independent pattern formation of nanorod and nanoparticle swarms under an oscillating field. *ACS Nano* **15**, 4429–4439 (2021).
34. J. Yu, B. Wang, X. Du, Q. Wang, L. Zhang, Ultra-extensible ribbon-like magnetic microswarm. *Nat. Commun.* **9**, 3260 (2018).
35. H. Zhou, C. C. Mayorga-Martinez, S. Pané, L. Zhang, M. Pumera, Magnetically driven micro and nanorobots. *Chem. Rev.* **121**, 4999–5041 (2021).
36. R. Cheng, W. Huang, L. Huang, B. Yang, L. Mao, K. Jin, Q. ZhuGe, Y. Zhao, Acceleration of tissue plasminogen activator-mediated thrombolysis by magnetically powered nanomotors. *ACS Nano* **8**, 7746–7754 (2014).
37. Q. Wang, D. Jin, B. Wang, N. Xia, H. Ko, B. Y. M. Ip, T. W. H. Leung, S. C. H. Yu, L. Zhang, Reconfigurable magnetic microswarm for accelerating tPA-mediated thrombolysis under ultrasound imaging. *IEEE ASME Trans. Mechatron.* **27**, 2267–2277 (2022).
38. J. Chen, L. Wang, H. Xu, L. Xing, Z. Zhuang, Y. Zheng, X. Li, C. Wang, S. Chen, Z. Guo, Q. Liang, Y. Wang, Meningeal lymphatics clear erythrocytes that arise from subarachnoid hemorrhage. *Nat. Commun.* **11**, 3159 (2020).
39. N. Dhanesha, M. R. Chorawala, M. Jain, A. Bhalla, D. Thedens, M. Nayak, P. Doddapattar, A. K. Chauhan, Fn-EDA (fibronectin containing extra domain A) in the plasma, but not endothelial cells, exacerbates stroke outcome by promoting thrombo-inflammation. *Stroke* **50**, 1201–1209 (2019).
40. H. Li, Z. Yang, Q. Tang, Z. Shi, Y. Mao, Embolic stroke model with magnetic nanoparticles. *ACS Appl. Mater. Inter.* **13**, 43993–44001 (2021).
41. A. K. Dunn, Laser speckle contrast imaging of cerebral blood flow. *Ann. Biomed. Eng.* **40**, 367–377 (2012).
42. J. W. Goodman, *Speckle Phenomena in Optics: Theory and Applications* (SPIE, ed. 2, 2020); available at https://doi.org/10.1117/3.2548484.
43. A. K. Dunn, H. Bolay, M. A. Moskowitz, D. A. Boas, Dynamic imaging of cerebral blood flow using laser speckle. *J. Cereb. Blood Flow Metab.* **21**, 195–201 (2001).
44. M. M. R. de Oliveira, C. E. Ferrarez, T. M. Ramos, J. A. Malheiros, A. Nicolato, C. J. Machado, M. T. Ferreira, F. B. de Oliveira, C. F. P. M. de Sousa, P. H. V. Costa, S. Gusmao, G. Lanzino, R. D. Maestro, Learning brain aneurysm microsurgical skills in a human placenta model: Predictive validity. *J. Neurosurg.* **128**, 846–852 (2018).
45. Y. Wang, J. Shen, S. Handschuh-Wang, M. Qiu, S. Du, B. Wang, Microrobots for targeted delivery and therapy in digestive system. *ACS Nano* **17**, 27–50 (2023).
46. L. Wang, Z. Meng, Y. Chen, Y. Zheng, Engineering magnetic micro/nanorobots for versatile biomedical applications. *Adv. Intell. Syst.* **3**, 2000267 (2021).
47. J. Wang, Y. Dong, P. Ma, Y. Wang, F. Zhang, B. Cai, P. Chen, B.-F. Liu, Intelligent micro−/nanorobots for cancer theragnostic. *Adv. Mater.* **34**, e2201051 (2022).
48. F. Soto, J. Wang, R. Ahmed, U. Demirci, Medical micro/nanorobots in precision medicine. *Adv. Sci.* **7**, 2002203 (2020).
49. H. Xu, M. Medina-Sánchez, M. F. Maitz, C. Werner, O. G. Schmidt, Sperm micromotors for cargo delivery through flowing blood. *ACS Nano* **14**, 2982–2993 (2020).
50. M. Wan, Q. Wang, R. Wang, R. Wu, T. Li, D. Fang, Y. Huang, Y. Yu, L. Fang, X. Wang, Y. Zhang, Z. Miao, B. Zhao, F. Wang, C. Mao, Q. Jiang, X. Xu, D. Shi, Platelet-derived porous nanomotor for thrombus therapy. *Sci. Adv.* **6**, eaaz9014 (2020).
51. F. Zhang, J. Zhuang, Z. Li, H. Gong, B. E.-F. de Ávila, Y. Duan, Q. Zhang, J. Zhou, L. Yin, E. Karshalev, W. Gao, V. Nizet, R. H. Fang, L. Zhang, J. Wang, Nanoparticle-modified microrobots for in vivo antibiotic delivery to treat acute bacterial pneumonia. *Nat. Mater.* **21**, 1324–1332 (2022).
52. D. Jin, K. Yuan, X. Du, Q. Wang, S. Wang, L. Zhang, Domino reaction encoded heterogeneous colloidal microswarm with on-demand morphological adaptability. *Adv. Mater.* **33**, e2100070 (2021).
53. D. Briers, D. Duncan, E. Hirst, S. Kirkpatrick, M. Larsson, W. Steenbergen, T. Stromberg, O. Thompson, Laser speckle contrast imaging: Theoretical and practical limitations. *J. Biomed. Opt.* **18**, 066018 (2013).
54. M. A. Malvindi, V. De Matteis, A. Galeone, V. Brunetti, G. C. Anyfantis, A. Athanassiou, R. Cingolani, P. P. Pompa, Toxicity assessment of silica coated iron oxide nanoparticles and biocompatibility improvement by surface engineering. *PLOS ONE* **9**, e85835 (2014).
55. Y. Dong, L. Wang, K. Yuan, F. Ji, J. Gao, Z. Zhang, X. Du, Y. Tian, Q. Wang, L. Zhang, Magnetic Microswarm composed of porous nanocatalysts for targeted elimination of biofilm occlusion. *ACS Nano* **15**, 5056–5067 (2021).
56. A. Aziz, M. Medina-Sánchez, N. Koukourakis, J. Wang, R. Kuschmierz, H. Radner, J. W. Czarske, O. G. Schmidt, Real-time IR tracking of single reflective micromotors through scattering tissues. *Adv. Funct. Mater.* **29**, 1905272 (2019).
57. G. Hong, A. L. Antaris, H. Dai, Near-infrared fluorophores for biomedical imaging. *Nat. Biomed. Eng.* **1**, 0010 (2017).
58. V. Ntziachristos, Going deeper than microscopy: The optical imaging frontier in biology. *Nat. Methods* **7**, 603–614 (2010).
59. B. Wang, K. F. Chan, K. Yuan, Q. Wang, X. Xia, L. Yang, H. Ko, Y.-X. J. Wang, J. J. Y. Sung, P. W. Y. Chiu, L. Zhang, Endoscopy-assisted magnetic navigation of biohybrid soft microrobots with rapid endoluminal delivery and imaging. *Sci. Robot.* **6**, eabd2813 (2021).
60. Y. Liu, G. Lin, G. Bao, M. Guan, L. Yang, Y. Liu, D. Wang, X. Zhang, J. Liao, G. Fang, X. Di, G. Huang, J. Zhou, Y. Y. Cheng, D. Jin, Stratified disk microrobots with dynamic maneuverability and proton-activatable luminescence for in vivo imaging. *ACS Nano* **15**, 19924–19937 (2021).
61. Q. Wang, X. Du, D. Jin, L. Zhang, Real-time ultrasound doppler tracking and autonomous navigation of a miniature helical robot for accelerating thrombolysis in dynamic blood flow. *ACS Nano* **16**, 604–616 (2022).
62. A. Aziz, M. Medina-Sánchez, J. Claussen, O. G. Schmidt, Real-time optoacoustic tracking of single moving micro-objects in deep phantom and ex vivo tissues. *Nano Lett.* **19**, 6612–6620 (2019).
63. T. Wei, J. Liu, D. Li, S. Chen, Y. Zhang, J. Li, L. Fan, Z. Guan, C.-M. Lo, L. Wang, K. Man, D. Sun, Development of magnet-driven and image-guided degradable microrobots for the precise delivery of engineered stem cells for cancer therapy. *Small* **16**, e1906908 (2020).
64. J. Law, X. Wang, M. Luo, L. Xin, X. Du, W. Dou, T. Wang, G. Shan, Y. Wang, P. Song, X. Huang, J. Yu, Y. Sun, Microrobotic swarms for selective embolization. *Sci. Adv.* **8**, eabm5752 (2022).
65. R. Nauber, S. R. Goudu, M. Goeckenjan, M. Bornhäuser, C. Ribeiro, M. Medina-Sánchez, Medical microrobots in reproductive medicine from the bench to the clinic. *Nat. Commun.* **14**, 728 (2023).
66. Y. Kim, E. Genevriere, P. Harker, J. Choe, M. Balicki, R. W. Regenhardt, J. E. Vranic, A. A. Dmytriw, A. B. Patel, X. Zhao, Telerobotic neurovascular interventions with magnetic manipulation. *Sci. Robot.* **7**, eabg9907 (2022).
67. T. Wang, H. Ugurlu, Y. Yan, M. Li, M. Li, A.-M. Wild, E. Yildiz, M. Schneider, D. Sheehan, W. Hu, M. Sitti, Adaptive wireless millirobotic locomotion into distal vasculature. *Nat. Commun.* **13**, 4465 (2022).
68. D. Jin, J. Yu, K. Yuan, L. Zhang, Mimicking the structure and function of ant bridges in a reconfigurable microswarm for electronic applications. *ACS Nano* **13**, 5999–6007 (2019).
69. L. Gao, J. Yu, Y. Liu, J. Zhou, L. Sun, J. Wang, J. Zhu, H. Peng, W. Lu, L. Yu, Z. Yan, Y. Wang, Tumor-penetrating peptide conjugated and doxorubicin loaded T_1-T_2 dual mode MRI contrast agents nanoparticles for tumor theranostics. *Theranostics* **8**, 92–108 (2018).
70. J. Piella, N. G. Bastús, V. Puntes, Size-controlled synthesis of sub-10-nanometer citrate-stabilized gold nanoparticles and related optical properties. *Chem. Mater.* **28**, 1066–1075 (2016).
71. S. Jeong, H. Choi, G. Go, C. Lee, K. S. Lim, D. S. Sim, M. H. Jeong, S. Y. Ko, J.-O. Park, S. Park, Penetration of an artificial arterial thromboembolism in a live animal using an intravascular therapeutic microrobot system. *Med. Eng. Phys.* **38**, 403–410 (2016).
72. S. Martel, O. Felfoul, J.-B. Mathieu, A. Chanu, S. Tamaz, M. Mohammadi, M. Mankiewicz, N. Tabatabaei, MRI-based medical nanorobotic platform for the control of magnetic nanoparticles and flagellated bacteria for target interventions in human capillaries. *Int. J. Rob. Res.* **28**, 1169–1182 (2009).
73. E. B. Steager, M. Selman Sakar, C. Magee, M. Kennedy, A. Cowley, V. Kumar, Automated biomanipulation of single cells using magnetic microrobots. *Int. J. Rob. Res.* **32**, 346–359 (2013).
74. Z. Wu, J. Troll, H.-H. Jeong, Q. Wei, M. Stang, F. Ziemssen, Z. Wang, M. Dong, S. Schnichels, T. Qiu, P. Fischer, A swarm of slippery micropropellers penetrates the vitreous body of the eye. *Sci. Adv.* **4**, eaat4388 (2018).

75. D. Li, D. Dong, W. Lam, L. Xing, T. Wei, D. Sun, Automated in vivo navigation of magnetic-driven microrobots using OCT imaging feedback. *I.E.E.E. Trans. Biomed. Eng.* **67**, 2349–2358 (2020).

Acknowledgments: We thank the support from Multi-Scale Medical Robotics Centre (MRC), InnoHK, at the Hong Kong Science Park and the SIAT-CUHK Joint Laboratory of Robotics and Intelligent Systems. We also thank T. Lam and K. Lai for support. **Funding:** This work was supported by the Hong Kong Research Grants Council (RGC) with project nos. RFS2122-4S03, R4015-21, C1134-20GF, E-CUHK401/20, 14300621, and 14301122; the ITF project with project no. MRP/036/18X funded by the HKSAR Innovation and Technology Commission (ITC); the National Natural Science Foundation of China with project no. 52205590 and no. 22102104; the Natural Science Foundation of Shenzhen University with grant no. 000002110712; the Guangdong Basic and Applied Basic Research Foundation (2021A1515010672); the Natural Science Foundation of Jiangsu Province with project no. BK20220834; and the Start-up Research Fund of Southeast University with project no. RF1028623098. **Author contributions:** Conceptualization: Qinglong Wang, B.Y.M.I., H.K., and L.Z. Methodology: Qinglong Wang and Qianqian Wang. Investigation: Qinglong Wang, K.F.C., Z.N., J.J., Y.W., L.S., S.J., B.W., Qianqian Wang, B.Y.M.I., H.K., T.W.H.L., P.W.Y.C., and S.C.H.Y. Visualization: Qinglong Wang and Qianqian Wang. Supervision: L.Z. Writing—original draft: Qinglong Wang. Writing—review and editing: Qinglong Wang, Qianqian Wang, B.Y.M.I., and L.Z. **Competing interests:** The authors declare that they have no competing interests. **Data and materials availability:** All data needed to support the conclusions of this manuscript are included in the main text or Supplementary Materials. Code is available at https://zenodo.org/records/10522671.

Submitted 16 February 2023
Accepted 26 January 2024
Published 21 February 2024
10.1126/scirobotics.adh1978

Science Robotics

Tracking and navigation of a microswarm under laser speckle contrast imaging for targeted delivery

Qinglong Wang, Qianqian Wang, Zhipeng Ning, Kai Fung Chan, Jialin Jiang, Yuqiong Wang, Lin Su, Shuai Jiang, Ben Wang, Bonaventure Yiu Ming Ip, Ho Ko, Thomas Wai Hong Leung, Philip Wai Yan Chiu, Simon Chun Ho Yu, and Li Zhang

Sci. Robot. **9** (87), eadh1978. DOI: 10.1126/scirobotics.adh1978

Editor's summary

Micro- and nanorobots have been widely proposed for various medical applications, including drug delivery and thrombolysis. However, tracking these swarms of robots in real time has been challenging, especially for imaging modalities that rely on extended exposure to ionizing radiation. Wang *et al*. report on the use of laser speckle contrast imaging to track a swarm of magnetic nanorobots within blood vessels in real time and guide their endovascular navigation. The authors demonstrated the potential for high contrast imaging and navigation of the swarm of nanorobots in stagnant and flowing blood environments ex vivo and in vivo. The findings offer an opportunity for improvements in targeted endovascular delivery. —Amos Matsiko

Science Robotics (ISSN 2470-9476) is published by the American Association for the Advancement of Science. 1200 New York Avenue NW, Washington, DC 20005. The title *Science Robotics* is a registered trademark of AAAS.